Astronomy & Astrophysics manuscript no. main
July 1, 2026
©ESO 2026

arXiv:2606.30746v1 [astro-ph.GA] 29 Jun 2026

Introducing AuriGLOBES: the effect of compressive tides, compact object-induced mass loss, and size evolution on modelling globular clusters

Pablo Contreras Guerra[1,2], Robert J. J. Grand[3], Marta Reina-Campos[4,5,6], and Claudio Dalla Vecchia[1,2]

[1] Instituto de Astrofísica de Canarias, c/ Via Lactea s/n, 38205 La Laguna, Spain
[2] Departamento de Astrofísica, Universidad de La Laguna, 38206 La Laguna, Spain
[3] Astrophysics Research Institute, Liverpool John Moores University, 146 Brownlow Hill, Liverpool L3 5RF, UK
[4] Instituto Galego de Física de Altas Enerxías, Universidade de Santiago de Compostela, 15782 Santiago de Compostela, Galicia, Spain
[5] Canadian Institute for Theoretical Astrophysics (CITA), University of Toronto, 60 St. George Street, Toronto, Ontario M5S 3H8, Canada
[6] Department of Physics & Astronomy, McMaster University, 1280 Main Street West, Hamilton, L8S 4M1, Canada

Received, 20XX

ABSTRACT

Globular clusters (GCs) are long time survivors of galaxy assembly and evolution yet their emergence from an initial cluster population is still poorly constrained. We present the Auriga GLOBular clustEr Simulations (AuriGLOBES) a physically motivated subgrid model for star cluster (SC) formation and evolution that includes enhanced mass loss from compact object remnants. With this model, implemented in the Auriga cosmological galaxy formation model, we run a suite of zoom-in cosmological simulations comprising 9 Milky Way mass and 5 lower mass galaxies. We demonstrate that our model produces plausible GC populations compared to the Milky Way/M31 systems and reproduces the empirical GC system mass – halo mass relation within a 2σ scatter. We show that the formation of SCs in tidally compressive, high-pressure gas in addition to enhanced mass loss from compact object remnants heating is required to capture the transformation of an initial Schechter mass function to the characteristic observed GC mass function in the Milky Way/M31 systems. The resulting GC populations show spatial and metallicity distributions qualitatively similar to the Milky Way/M31 systems, as well as a variety of age distributions that correlate with the star formation history of the simulated galaxies. However, the peak of the age distribution of Milky Way GCs is older than any of our simulated Milky Way-mass galaxies, which is attributed to unrepresented star formation and galaxy assembly histories. AuriGLOBES represents a reliable framework for the study of GC populations through cosmic history and a robust foundation for future applications for a model of stellar streams arising from GCs disruption.

Key words. galaxies: star clusters: general - globular clusters: general - galaxies: formation - galaxies: evolution - methods: numerical

1. Introduction

Star clusters (SCs) are fundamental building blocks of galaxies and powerful tracers of their formation and assembly history. Among these, globular clusters (GCs) are particularly puzzling due to their old ages, $\gtrsim$ 6 Gyr (e.g. Strader et al. 2005; Forbes & Bridges 2010; VandenBerg et al. 2013), and near universal presence in galaxies across a wide mass range (Harris 1991; Brodie & Strader 2006; Harris et al. 2017; Forbes et al. 2018; Dornan & Harris 2025; Forbes & Gannon 2025). The old ages of many GCs mean they formed early in the universe and survived until low-redshift, offering a unique window into the physical conditions of high-redshift star formation and the hierarchical growth of galaxies. Their metallicities, ages, kinematics, and spatial distributions encode information about their host galaxy assembly, making them valuable tools for studying both early galaxy formation and late-time galactic dynamics (e.g. Searle & Zinn 1978; Ibata et al. 1994; Forbes & Bridges 2010).

How the present-day GC population emerged from its initial cluster population remains an open question. Observations of GC-like young massive clusters (YMCs) forming in the local Universe (e.g. Holtzman et al. 1992; Whitmore & Schweizer 1995; Zepf et al. 1999; Adamo et al. 2017) have suggested that SC formation is a byproduct of star formation in high-pressure regions (e.g. Harris & Pudritz 1994; Elmegreen & Efremov 1997; Kruijssen 2014). In this picture, GCs are the long-term survivors of YMCs formed early in the universe. This has been reinforced by recent JWST observations of compact, dense, clusters and clumps at high redshift, i.e. $0.5 < z < 10$, in the context of sites of proto-GCs formation (e.g. Adamo et al. 2024; Mowla et al. 2024; Claeyssens et al. 2025, 2026). The mass functions (MFs) of YMCs follow a power-law with an exponential cutoff at high masses (Portegies Zwart et al. 2010; Johnson et al. 2017; Adamo et al. 2020; Wainer et al. 2022). Furthermore, this MF seems to be already in place from the early universe throughout cosmic history (Claeyssens et al. 2026). In contrast, the GC mass function (GCMF) across galaxies is remarkably uniform and log-normal-like, with the peak, at $M \sim 10^5 M_\odot$, weakly depending on the host galaxy stellar mass and galactocentric radius (Harris 1991; Jordán et al. 2007). This suggests a transformation driven by dynamical evolution –including mass loss from stellar evolution, internal two-body relaxation, and tidal stripping– affecting preferentially low-density clus-

ters (Fall & Zhang 2001; Vesperini 2001; Elmegreen & Hunter 2010; Kruijssen 2015; Gieles & Gnedin 2023).

Capturing this transformation within a full cosmological framework is a major challenge due the vast dynamic range involved. The formation and evolution of SCs depend on parsec-scale processes, yet these must be modeled within their host galaxies evolving on kiloparsec and gigayear scales. Different approaches have been used to tackle this issue, with coarser methods allowing for wider cosmic time and larger number of galaxies to be explored.

First, high-resolution simulations with improved physics prescriptions have allowed to resolve the formation of clumps, proto clusters, and star clusters at high redshift (e.g. Mandelker et al. 2014; Kim et al. 2018; Ma et al. 2020; Williams et al. 2025), in galaxy mergers (e.g. Lahén et al. 2020; Li et al. 2022), and in dwarf galaxy systems (e.g. Gutcke 2024; Deng et al. 2024; Taylor et al. 2025). These simulations, however, are computationally extremely expensive and are usually limited to high redshifts and/or small volumes. Second, semi-analytic models offer computationally efficient frameworks to follow SCs formation and disruption across cosmic time by populating N-body, or full galaxy simulations, with SCs via post-processing (e.g. Renaud et al. 2017; Creasey et al. 2019; Phipps et al. 2020; Halbesma et al. 2020; Valenzuela et al. 2021; Rodriguez et al. 2023; Chen & Gnedin 2024a; De Lucia et al. 2024). Unlike models baked in galaxy simulations, these do not require complete reruns allowing to simulate SCs populations in large samples of galaxies and an efficient exploration of model parameters. Nevertheless, these could represent an incomplete SC model from not having the full information of the tidal environment shaping their disruption at all times.

Third, subgrid models embed simplified prescription for SCs formation and evolution directly within cosmological galaxy simulations enabling a consistent interaction between the SCs and their host galaxies. The results, however, can be sensitive to the specific galaxy model of choice, interstellar medium (ISM) structure, or disruption mechanisms/prescriptions. Important contributions under this approach include the models of Li et al. (2017, 2018); Li & Gnedin (2019), which use sink particle techniques to model SC formation in giant molecular clouds (GMC), the E-MOSAICS project (Pfeffer et al. 2018; Kruijssen et al. 2019a) including the MOSAICS[1] model for cluster formation and evolution (Kruijssen & Lamers 2008; Kruijssen 2009; Kruijssen et al. 2011) in a rerun of the EAGLE[2] simulations (Crain et al. 2015; Schaye et al. 2015), and the EMP-Pathfinder simulations (Reina-Campos et al. 2022a, 2023) implementing an updated MOSAICS prescription under a new galaxy formation model that includes a cold, dense phase of the ISM.

Despite significantly different numerical setups and physical processes included, previous efforts are demonstrating that the process of regular cluster formation, combined with that of hierarchical galaxy assembly, produce diverse populations of SCs that broadly resemble the observed clusters in the Local Universe. However, as highlighted in Reina-Campos et al. (2022a), uncertainties in the formation and evolution of SCs produce degeneracies in several of their properties, like their mass distribution (see their fig. 8). In particular, matching any observed GCMF involves considerations on the ability to capture tidal disruption (e.g. Pfeffer et al. 2018; Li & Gnedin 2019; Rodriguez et al. 2023; Reina-Campos et al. 2022a), assumed SCs size/density prescriptions (e.g. Reina-Campos et al. 2023), and compatible assembly histories (e.g Chen & Gnedin 2024a). These uncertainties motivate to further study the formation and evolution of GCs under different galaxy formation models.

To this end, we present AuriGLOBES: Auriga GLOBular clustEr Simulations, a physically motivated subgrid model for the formation and evolution of star clusters implemented within the Auriga suite of cosmological zoom-in simulations. These are evolved in a Lambda Cold Dark Matter (ΛCDM) cosmology including a comprehensive galaxy formation physics model giving predictions that compare well with many observed scaling relations, such as the Tully-Fisher relation, the star-forming main sequence, and HI gas fraction/disc thickness (Grand et al. 2017, 2024). Our model incorporates four updates to the SC modelling used in previous works:

First, *(i)* it includes a novel criterion for constraining SC formation to tidally compressive gas environments only and *(ii)* implements an empirically-motivated initial mass-radius relation (MRR). Such compressive regions conductive to the formation of gravitationally bound clusters (Renaud et al. 2014, 2015) are consistent with theoretical expectations and observations linking cluster formation to dynamically driven, high-pressure environments (Renaud et al. 2009; Whitmore et al. 2010; Johnson et al. 2015). The SCs are then dynamically evolved in mass through two-body relaxation and tidal shocks. In particular, *(iii)* our two-body relaxation mass loss prescription accounts for the enhanced two-body scattering expected from clusters that retain a fraction of their compact stellar remnants. The inclusion of this enhancement is motivated by recent studies showing that SCs could retain populations of black holes (BHs) and their role as a source of energy for the clusters dynamical evolution (Gieles & Gnedin 2023; Della Croce et al. 2024). This is further motivated by increasing detections of BHs in MW GCs (e.g. Giesers et al. 2018; Kremer et al. 2020; Weatherford et al. 2020; Dickson et al. 2024) and extragalactic GCs (e.g. Maccarone et al. 2007, 2011; Barnard et al. 2012; Saracino et al. 2022). Finally, *(iv)* we implement a size evolution prescription that is coupled to the mass evolution of the SCs. Together, these ingredients provide a reliable framework to model the formation and long-term evolution of SC populations in a cosmological context.

This paper is structured as follows: in section 2 we describe the simulation setup including the description of the Auriga simulations and of our AuriGLOBES model; in section 3 we present the suite of simulations run with our model and in section 4 we show the results of the simulated SC and GC populations; finally, we give the discussion and conclusions in sections 5 and 6.

2. Simulation Setup

In this section, we describe our AuriGLOBES sub-grid SC model, which is implemented into the Auriga galaxy formation model (Grand et al. 2017). We first describe the Auriga model in section 2.1, and then give a full description of AuriGLOBES in section 2.2. The complete schematic of the model workflow, and its relation with Auriga, is shown in fig. 1.

2.1. The Auriga galaxy formation model

The Auriga formation model is implemented in the second-order accurate gravo-magnetohydrodynamic (MHD) code AREPO (Springel 2010), which follows MHD and collisionless dy-

[1] MOdelling Star cluster population Assembly in Cosmological Simulations

[2] Evolution and Assembly of GaLaxies and their Environments

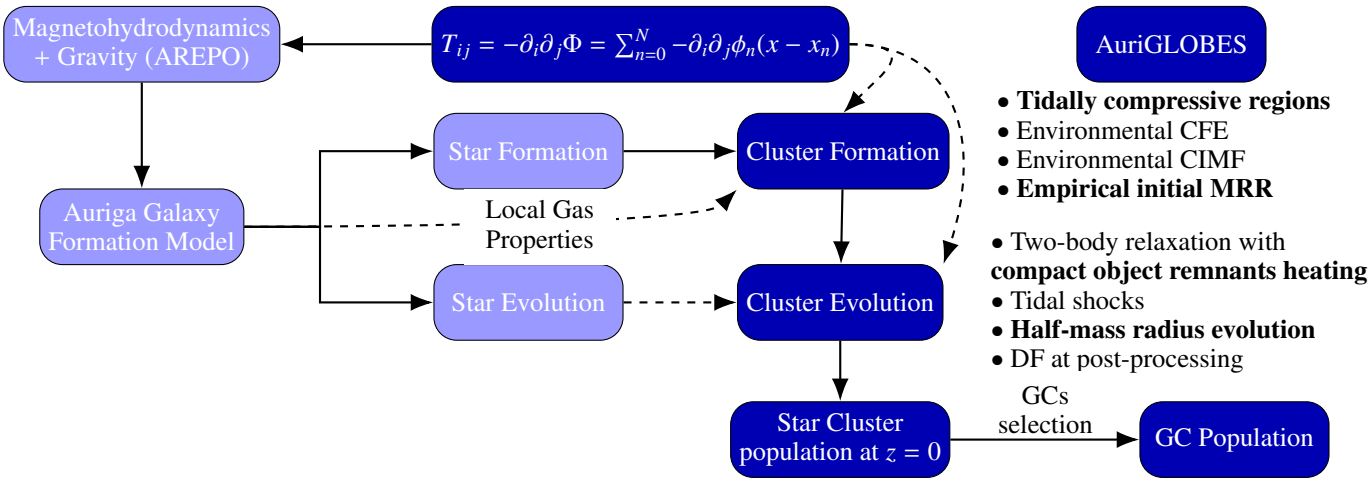


Fig. 1: The AuriGLOBES star cluster formation and evolution model. The base simulation code and the Auriga galaxy formation model, with star formation and evolution stages, are depicted in lightblue boxes. The AuriGLOBES extension to the base simulation is depicted in darkblue boxes. Continuous arrows represent a direct relation while dashed arrows represent a dependency relation. Bold fonts highlight extensions with respect to previous models. The used acronyms are: cluster formation efficiency (CFE), cluster initial mass function (CIMF), mass radius relation (MRR), dynamical friction (DF), and globular clusters (GCs).

namics in a cosmological context. AREPO calculates gravitational forces with a standard Tree Particle-Mesh method (Springel 2005) comprising a hierarchical oct-tree algorithm (Barnes & Hut 1986) for short range forces and a fast Fourier treatment for long range forces. The timestep is adaptive and MHD is solved in an unstructured Voronoi mesh that moves approximately with the fluid. This way, AREPO performs as a "hybrid" Eulerian and Langrangian code reducing errors accumulating from large relative bulk velocities inherent to galaxy formation (Wadsley et al. 2008) while retaining the ability to capture shocks to a good accuracy (Schaal & Springel 2015; Schaal et al. 2016).

The simulations follow a comprehensive galaxy formation model including the evolution of gas, dark matter, stars, and BHs. It is described in detail in Grand et al. (2017), and builds on top of models presented in Vogelsberger et al. (2013) and Marinacci et al. (2014). The model implements:

- a pressurized two phase ISM model consisting of cold, dense, clouds embedded in a hot, ambient medium Springel & Hernquist (2003),
- stochastic star formation for dense ISM gas above a threshold density of $n_{\rm th} = 0.13$ cm^{-3} with a Chabrier (2003) initial mass function (IMF). This threshold is derived from the parameters of the two gas phases and a desired star formation time-scale of $t_{\rm SF} = 2.2$ Gyr,
- primordial and metal-line cooling and heating from a uniform ultraviolet background radiation field (Faucher-Giguère et al. 2009),
- stellar evolution from asymptotic giant branch stars and supernovae type Ia and II with a stellar feedback scheme for thermal and kinetic energy injection,
- supermassive black holes seeding and growth,
- active galactic nuclei thermal feedback in quasar and radio modes, and
- magnetic fields seeded uniformly at the starting redshift of the simulation at a comoving strength of 10^{-14} G (Pakmor et al. 2017).

The Auriga galaxy formation model has been employed to run large suites of cosmological MHD simulations for the formation and evolution of Milky Way-mass and dwarf-mass galaxies in the ΛCDM cosmogony (Grand et al. 2024). The simulations use the "zoom-in" technique, which resimulates galaxy halos from the Eagle Dark Matter Only simulation of comoving side length 100 cMpc (L100N1504 in Schaye et al. 2015, $1.15 \times 10^7 M_\odot$ mass resolution) at high resolution. The initial conditions of these resimulations are created with the public Gaussian white noise field realization Panphasia (Jenkins 2013) adopting the cosmological parameters from Planck Collaboration et al. (2014), i.e. $\Omega_{\rm m} = 0.307$, $\Omega_{\rm b} = 0.048$, $\Omega_\Lambda = 0.693$, $\sigma_8 = 0.8288$, and Hubble constant of $H_0 = 100h$ km s^{-1} Mpc^{-1}, where $h = 0.6777$. For each identified halo, the particles inside four times its virial radius at $z = 0$ where traced back to their initial position at $z = 127$ and resampled to a higher mass resolution while lowering the resolution of particles at larger distances. This reduces computational cost while maintaining the correct cosmological tidal field. For more details on the Auriga simulation suite, please refer to Grand et al. (2017, 2024). In this paper, we apply our SCs formation and evolution model, described in the next subsection, by re-running some of these cosmological simulations (see section 3).

2.2. The AuriGLOBES sub-grid star cluster model

The SCs formation and evolution model largely follows subgrid prescriptions available in the literature (e.g. Pfeffer et al. 2018; Reina-Campos et al. 2022a) adapting them to work with our galaxy formation setting and extending the covered physical processes to cover compressive natal environments, empirical initial sizes, enhanced mass loss from compact object heating, and size evolution. In the following subsections, we describe in detail the physics and numerical implementation of the AuriGLOBES SC model.

2.2.1. Cluster Formation

In our fiducial model, a newly created star particle is eligible to host SCs based on the properties of the natal gas cell. In addition to high gas density and pressure leading to bound systems to likely form, we also require the gas environment to be tidally

compressive. The latter is determined from calculating the tidal tensor, **T**. We do it in a similar way as in Grudić & Hopkins (2020), by using the linearity of **T** to sum the contributions of each particle in the simulation:

$$T_{ij} = \sum_{n=0}^{N} -\partial_i \partial_j \Phi_n(\mathbf{x} - \mathbf{x}_n) = \sum_{n=0}^{N} \partial_i \mathbf{g}_{n,j}(\mathbf{x} - \mathbf{x}_n), \quad (1)$$

where Φ_n is the gravitational potential, and $\mathbf{g}_{n,j}$ the acceleration (j-th component) contribution of the particle n as a function of the separation $\mathbf{x} - \mathbf{x}_n$, and the partial derivatives are with respect to the target position $\mathbf{x}$. The evaluation of the tidal tensor is done in the same tree walk as the evaluation of $\mathbf{g}$.

Once **T** is defined[3], its eigenvalues λ_i describe whether the gravity field stretches or squeezes a region in each of the three spatial directions: negative values mean that gravity is compressive in a given direction, whereas positive values reflect the opposite. Therefore, whether the medium is compressive or not is ensured by having all three negative eigenvalues. We further strengthen this condition to having all three eigenvalues less than a certain negative threshold, i.e. $\forall \lambda_i \leq -1$ Gyr^{-2}. This threshold was chosen by visually inspecting the tidal tensor eigenvalues distribution and finding that the negative eigenvalues are generally well below this value (see appendix B.2).

Once a star particle is identified to be born in a tidally compressive region, the formation of SCs is determined by three ingredients: *(i)* the Cluster Formation Efficiency (CFE, Γ), i.e. the fraction of star formation happening in bound structures (Bastian 2008), estimated from the physical properties of the parent gas cell; *(ii)* a locally defined Cluster Initial Mass Function (CIMF) from which the individual SC masses are drawn; and *(iii)* an empirical initial MRR from which the individual SC sizes are determined. These are explained in the following paragraphs. As previous papers have reported, the numerical details of how star formation is modelled affect the resulting cluster population (e.g. Pfeffer et al. 2018; Reina-Campos et al. 2022a). Thus, we perform additional simulation tests to assess the influence of including or not this compressive criterion (see section section 3.1).

We estimate the CFE by implementing the Kruijssen (2012) model, which estimates the fraction of star formation happening in bound structures from integrating the density spectrum of the ISM. In particular, we use the model formulation based on the local properties of the gas, i.e. $f_{\rm bound} = \Gamma(\rho_{\rm g}, \sigma_{\rm loc}, c_s)$, with $\rho_{\rm g}$ the gas density, $\sigma_{\rm loc}$ the gas velocity dispersion, and c_s its sound speed. Equivalent to E-MOSAICS (Pfeffer et al. 2018), we estimate the one-dimensional velocity dispersion from $\sigma_{\rm loc} = \sqrt{P_{\rm g}/\rho_{\rm g}}$, with $P_{\rm g}$ the local gas pressure, and assume a thermal sound speed corresponding to a cold interstellar gas at ~ 10 K, i.e. $c_{\rm s} = 0.3\,{\rm km\,s^{-1}}$. The implementation of the local formulation of Kruijssen (2012) model is justified given that the local gas properties are a good description of the global state of the gas, mainly from the ISM model not explicitly modeling a cold, clumpy, structure.

The fraction Γ sets the mass budget for SC masses to be drawn from the CIMF which is given by a Schechter (1976) function

$$\mathrm{d}N \propto m^{-\alpha} \exp\left(-m/m_{\rm cl,max}\right) \mathrm{d}m, \quad (2)$$

where $\alpha \simeq 2$ (Zhang & Fall 1999) is the power-law index, $m_{\rm cl,max}$ the CIMF truncation mass, and m the individual SC mass. This CIMF has been shown to be consistent with populations of Young Star Clusters (YSC) in the local Universe (Portegies Zwart et al. 2010; Johnson et al. 2017; Adamo et al. 2020; Wainer et al. 2022). High-resolution simulations following star-by-star compact SC formation agree with this power-law, whereas the exponential cut-off has been difficult to characterize due the size-of-sampling effect (e.g. Lahén et al. 2020; Andersson et al. 2024; Pascale et al. 2025).

The truncation mass is set by the mass of the GMC from which clusters originate (Kruijssen 2014), $M_{\rm GMC,max}$. To estimate this, we use the environment dependent model of Reina-Campos & Kruijssen (2017), i.e.

$$m_{\rm cl,max} = \epsilon \Gamma M_{\rm GMC,max} \; ; \; M_{\rm GMC,max} = f_{\rm coll} M_{\rm T}, \quad (3)$$

where $\epsilon = 0.1$ is the integrated star formation efficiency for an entire molecular cloud[4] (Duerr et al. 1982; Murray 2011; Kruijssen et al. 2019c; Sun et al. 2023), $M_{\rm T}$ is the Toomre (1964) mass, i.e. the highest mass on a region that can collapse under its own gravity, and $f_{\rm coll}$ is the collapse fraction before stellar feedback stops this process:

$$f_{\rm coll} = \min\left(1, \frac{t_{\rm fb,g}}{t_{\rm ff,2D}}\right)^4, \quad (4)$$

where $t_{\rm fb,g}$ is the gas feedback time-scale, and $t_{\rm ff,2D}$ the two-dimensional cloud free-fall time. Following Kruijssen (2012), the gas feedback time-scale is

$$t_{\rm fb,g} = \frac{t_{\rm sn}}{2}\left(1 + \sqrt{1 + \frac{4 t_{\rm ff} \sigma_{\rm loc}^2}{\phi_{\rm fb} \epsilon_{\rm ff} t_{\rm sn}^2}}\right), \quad (5)$$

where $t_{\rm ff} = \sqrt{3\pi/32 G \rho_{\rm g}}$ is the gas free-fall time, $\epsilon_{\rm ff} = 0.012$ the star formation efficiency per free-fall time (Elmegreen 2002; Utomo et al. 2018; Grisdale et al. 2019), $t_{\rm sn} = 3$Myr is the typical time of the first supernova (Ekström et al. 2012), and $\phi_{\rm fb} = 0.16$ cm^{2}s^{-3} is the rate of energy injection per unit stellar mass into the ISM from feedback of a simple stellar population with a normal IMF (Kruijssen 2012). Lastly, the cloud free-fall time is defined as

$$t_{\rm ff,2D} = \frac{\sqrt{2\pi}}{\kappa}, \quad (6)$$

where κ is the epicyclic frequency that is computed from the tidal tensor at the location of the particle (see appendix B.1), as demonstrated by Pfeffer et al. (2018) and Reina-Campos et al. (2022a).

The Toomre mass is obtained from the parent gas cell for each new star particle through

$$M_{\rm T} = 4\pi^5 G^2 \frac{\Sigma_{\rm g}^3}{\kappa^4}, \quad (7)$$

where $\Sigma_{\rm g}$ is the local surface gas density estimated assuming hydrostatic equilibrium, i.e. equating the mid-plane pressure of an equilibrium disc to the pressure of the parent gas cell (Krumholz & McKee 2005):

$$\Sigma_{\rm g} = \sqrt{\frac{2 P_{\rm g}}{\pi G \phi_P}}, \quad (8)$$

[3] Note that long range, Fourier based, gravitational contributions are not taken into account for the tidal tensor calculus in favor of decreasing the computational time. We tested its inclusion and found negligible differences in the resulting tidal tensor. Both the test of the correct calculation of **T** and how negligible is the error when ignoring long range contributions are shown in the appendices B.1 and B.2.

[4] As noted by Pfeffer et al. (2018), the variation of ϵ estimates is much smaller than the dynamical range of the product $\Gamma M_{\rm GMC,max}$ making it reasonable to set as a constant.

with ϕ_P being the contribution of the gravity of stars to the mid-plane pressure. Following Pfeffer et al. (2018), this contribution is expressed as

$$\phi_P = 1 + \frac{\sigma_g}{\sigma_\star}\left(\frac{1}{f_{gas}} - 1\right), \tag{9}$$

with f_{gas} the gas mass fraction, and σ_g ($\sigma_\star$) the velocity dispersion of the gas (stars) in the vicinity region where ϕ_P is determined. This region is up to three times the parent gas cell smoothing length until a minimum of 64 gas cells are enclosed.

Clusters are formed by stochastically drawing from the CIMF. The number of clusters expected to form in a new star particle of mass $m_\star$ is given by the mass budget defined by Γ over the mean cluster mass, i.e. $N_{clus} = \Gamma m_\star / \bar{m}_{cl}$. This mean cluster mass is defined by integrating the normalized CIMF over the mass range for cluster formation:

$$\bar{m}_{cl} = \int_{10^2 M_\odot}^{10^8 M_\odot} m \frac{dN}{dm} dm. \tag{10}$$

Note that the mass range is set to be consistent with YSCs in the Local Universe (e.g. Brown & Gnedin 2021). Finally, the actual number of cluster masses to be drawn from the CIMF is defined from a Poisson distribution with the mean given by N_{clus}. While the low limit to draw masses is $10^2\,M_\odot$, clusters below $5{\times}10^3\,M_\odot$ are discarded to lower the memory consumption. This is justified given that all of these low mass clusters are expected to disrupt shortly after their formation ($<<$ 1 Gyr, Kruijssen et al. 2012). Due to the stochasticity of cluster formation, and depending on the mass resolution of the simulation, some of the star particles may contain cluster populations with a total mass exceeding their actual mass while others may contain no cluster populations. At the Auriga resolution "level 4", this accounts for $\sim$ 10% of the star particles that host SCs having a total mass in SCs higher than its mass; for most of the cases it is well bellow the parent star particle mass and close to the expected $\Gamma m_\star$ mass budget.

Finally, the created SCs are assigned an effective radius, R_{eff}, determining its half-mass radius, $r_{h,cl} = 4R_{eff}/3$. This is done by using the empirical mass-radius relation (MRR) for YSCs reported by Brown & Gnedin (2021). This relation corresponds to SCs in the LEGUS sample in the 1–10 Myr age range with its intrinsic scatter:

$$R_{eff} = 2.365\text{pc}\left(\frac{m_{cl}}{10^4 M_\odot}\right)^{0.18} \text{ with } \sigma_{R_{eff}} = 0.319 \text{ dex}, \tag{11}$$

where m_{cl} is the individual SC mass.

2.2.2. Cluster Evolution

Once SCs are formed, their dynamical evolution is immediately followed determining their mass loss coupled with their size evolution. The mass loss is determined by stellar evolution, two-body relaxation, and tidal shocks:

$$\frac{dm}{dt} = \left(\frac{dm}{dt}\right)_{sev} + \left(\frac{dm}{dt}\right)_{rlx} + \left(\frac{dm}{dt}\right)_{sh}. \tag{12}$$

The stellar evolution mass loss is directly inherited from the parent star particle evolution given by the Auriga model. For the dynamical mass loss mechanisms, we follow, or modify, available models applicable to sub-grid prescriptions (e.g. Gnedin & Ostriker 1997; Prieto & Gnedin 2008; Kruijssen et al. 2011; Alexander & Gieles 2012). Both two body relaxation and tidal shocks mass loss strongly depend on the underlying tidal field, eq. 1, as described below.

2.2.2.1. Two-body relaxation mass loss enhanced by compact object heating

The mass loss driven by two-body interactions leading to the evaporation of the cluster is estimated by[5]

$$\left(\frac{dm}{dt}\right)_{rlx} = -a\xi\frac{m}{t_{rh}}\left(\frac{m}{m_i}\right)^{-2/3}, \tag{13}$$

where ξ is the fraction of stars escaping the SC potential per relaxation time, a is a boosting parameter, t_{rh} is the relaxation time-scale at the half-mass radius, m is the current mass of the cluster, and $m_i \equiv \mu_{sev} m_0$ is the initial mass after the stellar evolution mass loss has occurred (Gieles & Gnedin 2023). For Auriga, μ_{sev} covers a range of $\mu_{sev} \approx 0.53$–1.

The relaxation time-scale, t_{rh}, is defined following Spitzer (1987):

$$t_{rh} = \frac{0.138\sqrt{N} r_h^{3/2}}{\sqrt{G\bar{m}}\ln(\gamma N)}, \tag{14}$$

with $N = m/\bar{m}$ the mean number of stars in the cluster, $\bar{m}$ the mean stellar mass in the cluster, and $\ln(\gamma N)$ the Coulomb logarithm with $\gamma \approx 0.11$(Giersz & Heggie 1994) for clusters of single-mass stars. For Auriga, which adopts a Chabrier (2003) IMF in the $0.1 \leq m/M_\odot \leq 100$ mass range, the mean stellar mass is $\bar{m} = 0.62\,M_\odot$. The escapers fraction ξ is estimated following the model described in the EMACSS prescription (Alexander & Gieles 2012; Gieles et al. 2014; Alexander et al. 2014) that fits the evaporation of N-body simulations of SCs submerged in a tidal field[6]:

$$\xi = \xi_0(1 - \mathcal{P}) + \frac{3}{5}\zeta\mathcal{P}, \tag{15}$$

where $\xi_0 = 0.0142$ is the fraction of stars escaping a SC in isolation (Alexander & Gieles 2012), $\zeta = 0.1$ is a dimensionless constant for the fractional energy change per relaxation time-scale (Hénon 1961, 1965; Gieles et al. 2011), and the effect of the tidal field is captured in the dimensionless evaporation rate $\mathcal{P}$ that is a function of the half-mass radius, the tidal radius, and the number of stars in the cluster (eq. 25 in Alexander & Gieles (2012) with the revised parameter values from Gieles et al. (2014)). The tidal radius is the boundary at which the gravitational acceleration due to the galactic potential equals the acceleration from the potential of the cluster and is given by

$$r_t = \left(\frac{Gm}{T}\right)^{1/3}. \tag{16}$$

where $T = -\partial^2\Phi/\partial r^2 + \Omega^2$ is the tidal field strength (King 1962), with the circular frequency, Ω. This is estimated from the tidal tensor eigenvalues as $T = \max(\lambda_i) + \Omega^2 = \max(\lambda_i) + 1/3\left|\sum_{i=1}^{3}\lambda_i\right|$, following Pfeffer et al. (2018) and Reina-Campos et al. (2022a).

The boosting parameter, $a = 1.5$, and the last factor in eq. 13, $(m/m_i)^{-2/3}$, account for the effect of compact object

[5] The canonical mass loss rate is given by $(dm/dt)_{rlx} = -\xi m/t_{rh}$

[6] Alexander et al. (2014) model revision provides a parametrization to include the effect of an evolving stellar mass spectrum making up the SCs where the relaxation timescale t_{rh} is modified to account for the effect of such a mass spectrum. It provides a recalibration of the parameters for multi-mass SCs accounting for the evolution of the mass spectrum and should, up to some degree, include the effect of the retention of compact object remnants. We performed tests using this model prescription with results showing an inconsistent behavior. For simplicity, we adopt the single-mass SCs prescription, with fewer parameters, and apply the compact objects correction afterwards.

remnants in the mass loss rates of SCs, following the parameterization given by Gieles & Gnedin (2023). These authors found that SCs retaining a fraction of their compact object remnants population experience an accelerated mass loss rate from two-body interactions and that this effect is fundamental in evolving an initial Schechter-like CIMF into a peaked GCMF consistent with observations (targeting the MW GC population, in particular). In addition, studies point to BHs populations being present in MW and extragalactic GCs (e.g. Maccarone et al. 2007, 2011; Barnard et al. 2012; Kremer et al. 2020; Weatherford et al. 2020; Saracino et al. 2022; Dickson et al. 2024) supporting the inclusion of this effect. Their parameterization follows from comparing N-body models of SCs forming and retaining compact object remnants in a galactic tidal field to the baseline N-body models of Baumgardt & Makino (2003), where SCs do not form BHs. We test in our results the effect of this enhancement comparing simulations with and without its inclusion (see section 3.1).

2.2.2.2. Tidal shocks mass loss

Tidal shocks, i.e. perturbations of the gravitational potential exerted by the passage through the disc or close encounters with dense structures, increase the kinetic energy of the stars in the clusters, reducing the binding energy of the cluster, and could cause stars to escape its potential (Ostriker et al. 1972; Spitzer 1987; Kundic & Ostriker 1995; Gnedin & Ostriker 1997; Murali & Weinberg 1997a,b,c; Gnedin et al. 1999a,b; Prieto & Gnedin 2008). The mass loss is given by the time-scale for tidal heating, $t_{\rm sh}$, to change the energy of the stars at the half-mass radius by an order of itself (Prieto & Gnedin 2008):

$$\left(\frac{{\rm d}m}{{\rm d}t}\right)_{\rm sh} = -\frac{m}{t_{\rm sh}}. \tag{17}$$

Following Prieto & Gnedin (2008), this time-scale is

$$t_{\rm sh} \equiv \frac{|E_{\rm h}|}{({\rm d}E_{\rm h}/{\rm d}t)_{\rm sh}} \simeq \frac{|E_{\rm h}|P}{2\langle\Delta E_{\rm h}\rangle} = \frac{3}{5}\frac{Gm}{r_{\rm h}^3}\frac{P}{I_{\rm tid}}, \tag{18}$$

where P is the time interval between shocks, $E_{\rm h}$ is the energy per unit mass at the half-mass radius, and $\langle\Delta E_{\rm h}\rangle$ its ensemble average. This energy is approximated as

$$|E_{\rm h}| = \frac{v_{\rm h}^2}{2} \approx \eta\frac{Gm}{2r_{\rm h}}, \tag{19}$$

with the proportionality constant $\eta \simeq 0.4$ (Spitzer 1987). Its ensemble average is given by

$$\langle\Delta E_{\rm h}\rangle = \frac{1}{2}\langle\Delta v\rangle^2 = \frac{1}{6}I_{\rm tid}r_{\rm h}^2, \tag{20}$$

where the tidal heating parameter, $I_{\rm tid}$, is defined by integrating the tidal tensor components through the duration of the shocks and summing over all its components:

$$I_{\rm tid} \equiv \sum_{i,j}\left(\int T_{ij}{\rm d}t\right)^2\left(1+\frac{\tau_{ij}^2}{t_{\rm dyn}^2}\right)^{-3/2}. \tag{21}$$

For each pair of coordinates, τ_{ij} is the shock duration[7], and $t_{\rm dyn} = \sqrt{8\pi r_{\rm h}^3/Gm}$ is the dynamical time-scale at the half-mass radius. The second term in eq. 21 accounts for the Weinberg (1994a,b,c) adiabatic correction for extended shocks describing the absorption of energy by adiabatically expanding the cluster.

2.2.3. Half-mass radius evolution

Following Reina-Campos et al. (2022a), we evolve the half-mass radius of SCs according to their mass evolution. As the stellar populations in SCs lose mass through stellar evolution, SCs experience an adiabatic expansion given by the inverse ratio of the parent star particle mass at the current and previous timestep, giving $({\rm d}r_{\rm h}/r_{\rm h})_{\rm sev} = |{\rm d}m_{\star,{\rm sev}}|/m_\star$. In addition to the adiabatic expansion, a dynamical evolution is also implemented where, having ${\rm d}m_{\rm rlx}$ and ${\rm d}m_{\rm sh}$, the size of the cluster is evolved accordingly. This evolution follows the density evolution derived by Gieles & Renaud (2016) extended to account for mass loss from two-body interactions (first derived in appendix E in Reina-Campos et al. 2023):

$$\left(\frac{{\rm d}r_{\rm h}}{r_{\rm h}}\right)_{\rm dyn} = \left(2-\frac{1}{f}\right)\frac{{\rm d}m_{\rm sh}}{m} + \left(2-\frac{\zeta}{\xi}\right)\frac{{\rm d}m_{\rm rlx}}{m}, \tag{22}$$

where $f = 3/5$ is the fraction of the energy gain of the *remaining bound* stars[8] translated into a change in density (Gieles & Renaud 2016). The choice of $f = 3/5$ means that the density remains constant after the mass loss, adjusting the size accordingly. We tried different parameters and the results show no strong dependence on this particular selection (see appendix C). Eq. 22 describes the shrinking of clusters due to shocks and their overall expansion from two-body interactions. Note, however, that in tidally limited scenarios, $\xi \simeq 3/5\zeta$ (from eq. 15), also gives cluster contraction from two-body interactions. Implementing a half-mass radius evolution model corresponding to the mass evolution allows to explore the different cluster disruption processes. As both two-body relaxation and tidal shocks mass loss models are dependent on $r_{\rm h}$, i.e. $t_{\rm rh} \propto r_{\rm h}^{3/2}$ and $t_{\rm sh} \propto r_{\rm h}^{-3}$, the size evolution of the SCs affects their survivability (e.g. Reina-Campos et al. 2023). To explore this effect, we compare simulations with and without evolving the half-mass radius (see section 3.1).

2.2.4. Dynamical friction

Finally, the effect of dynamical friction is estimated at post-processing with the same approach of Pfeffer et al. (2018), and Reina-Campos et al. (2022a). For a star particle hosting more than one SC, each one with its own mass, applying an on-the-fly dynamical friction treatment would result in star particles experiencing different forces from those of its SC population. This is specially relevant when the subgrid population has an important mass contrast between the clusters. Therefore, the effect is estimated by comparing the dynamical friction time-scale with the age of the cluster and assume SCs are disrupted whenever this time-scale is shorter. The dynamical friction time-scale is defined following Lacey & Cole (1993)

$$t_{\rm df} = \frac{f(\epsilon)}{2B(v_c/\sqrt{2\sigma})}\frac{\sqrt{2}\sigma\, r_c^2}{Gm\ln\Lambda}, \tag{23}$$

[7] For each component, the start (end) of a shock event is identified by finding a contrast of at least 88% with respect to the last recorded (last maximum) component value, and the integral runs over the full duration of the shock. The contrast is defined by the height ratio of a Gaussian distribution at 0.5σ and at the mean, defining a full width of 1σ.

[8] Not to be confused with the fraction of the energy gain translated into a mass loss following a shock event introduced by Gieles et al. (2006) using the same terminology but corresponding to all stars, i.e. including the ones that become unbound after the shock.

with r_c being the radius of a circular orbit with the same energy of the particle, σ the stellar velocity dispersion inside r_c, and v_c the circular velocity at r_c. The Coulomb logarithm is $\ln\Lambda = \ln(1 + M(r_c)/m)$, with $M(r_c)$ the total mass inside r_c, and $B(x) \equiv \mathrm{erf}(x) - 2x\exp(-x^2)/\sqrt{\pi}$. Finally, $\epsilon = J/J_c$ is the circularity parameter defined as the angular momentum relative to the angular momentum of a circular orbit of the same energy, while $f(\epsilon) = \epsilon^{0.78}$ defines the orbital eccentricity of the SC (Lacey & Cole 1993). This time-scale is estimated at every snapshot of the simulation data products and identified disrupted clusters are assigned a mass of zero from that snapshot onward.

3. The AuriGLOBES suite of simulations

In this paper we apply the AuriGLOBES sub-grid star cluster formation and evolution model to a subset of the simulated halos from the Auriga suite. The model is run at the baryonic mass resolution of $M_{\rm bary} \sim 5\times10^4\mathrm{M}_\odot$ and comoving softening length of $\epsilon_{\rm comov} \sim 750$ cpc up to a maximum physical softening length of $\epsilon_{\rm phys} \sim 375$ pc, referred as the "level 4" resolution.

3.1. Auriga re-simulations with AuriGLOBES

Firstly, we explore the effect of model choices on the resulting SC populations. For this we introduce six different model variations that we run in one of the halos, labeled as halo 6 in table 3 in Grand et al. (2024). This is a disc galaxy with a stellar mass of $\sim 5\times10^{10}\,\mathrm{M}_\odot$, similar to the estimated stellar mass of the MW, i.e. $\sim 2-6\times10^{10}\,\mathrm{M}_\odot$ (Licquia & Newman 2015; Lian et al. 2025). Starting from our `Fiducial` AuriGLOBES (see section 2.2), we "turn off" part of the model choices and analyze their effect on the SCs formation and evolution.

All the model variations, summarized in table 1, are: *(i)* `Fiducial` which includes all the physics described in section 2.2; *(ii)* `No BH heating` where we do not apply the mass loss enhancement due compact object heating; *(iii)* `No compressive criterion` where cluster formation is not constrained to tidally compressive regions only; and a *(iv)* `No added physics` model turning off both the BH heating and tidally compressive formation. In addition, we repeat the `Fiducial` model with two final variations: *(v)* `Enhanced shocks` arbitrarily enhancing the mass loss from tidal shocks by a factor of 10 during the full evolution of SCs; and *(vi)* `No size evolution` keeping the initial MRR but turning the half-mass radius evolution off. The purpose of these variations is to further test how the model is capturing the tidal disruption of SCs with an emphasis on the early disruption from their natal environments (Kruijssen et al. 2012) and the role of their half-mass density in their dynamical evolution.

Secondly, we run a suite of simulations comprising 9 halos with our `Fiducial` model. These simulated halos, in the $1\times10^{12}\mathrm{M}_\odot < M_{200}(z=0) < 2\times10^{12}\mathrm{M}_\odot$ mass range, are summarized in table 2. Thus covering a mass range similar to the MW and M31 systems with a variety of accretion and assembly histories that can impact the produced SC and GC populations. Note that the overall halo properties are slightly different compared to those listed in Grand et al. (2024), which is expected owing to phenomena such as the "Butterfly effect" (Genel et al. 2013; Keller et al. 2019; Pakmor et al. 2025a).

Table 1: Summary table for the halo 6 model variations.

Model	Formation	Mass loss
Fiducial	Compressive environments	BH enhanced
No BH heating	Compressive environments	Canonical evaporation
No compressive criterion	All environments	BH enhanced
No added physics	All environments	Canonical evaporation
Additional variations		
Model	Change description	
Enhanced shocks	Tidal shocks boosted by 10	
No size evolution	Keep initial MRR, $\mathrm{d}r_\mathrm{h}/\mathrm{d}t = 0$	

Notes. The columns are the model variation identifier (i), and the model variation description in (ii) and (iii).

Table 2: Summary table for the rerun halos at resolution "level 4", i.e. $M_{\rm bary} \sim 5\times10^4\mathrm{M}_\odot$ and $\epsilon_{\rm phys} \sim 375$ pc, with the AuriGLOBES model. We include the properties of the MW and M31 at the bottom for comparison.

Halo	M_{200} ($10^{10}\mathrm{M}_\odot$)	R_{200} (kpc)	M_* ($10^{10}\mathrm{M}_\odot$)	$M_{\rm GCs}$ ($10^6\mathrm{M}_\odot$)
6	104.7	214.1	5.1	197.6
14	157.6	245.3	11.8	248.3
18	120.8	224.5	9.4	266.6
22	100.9	211.5	7.0	66.3
23	156.7	244.9	9.3	258.5
24	155.9	244.4	9.5	316.3
26	153.6	243.2	10.4	455.8
27	178.3	255.6	10.7	389.9
28	156.2	244.6	10.6	273.8
Milky Way	108^{+20}_{-14}	–	2.6 ± 0.4	29.7
M31	250 ± 30	–	$10.3^{+2.3}_{-1.7}$	228.9

Notes. The columns are (i) halo identifier, (ii) total dynamical mass, (iii) halo radius, (iv) stellar mass, (v) total, cumulative, mass in GCs (see section. 3.2) older than 8 Gyr. MW properties: M_{200} from Cautun et al. (2020), $M_\star$ from Lian et al. (2025), and $M_{\rm GCs}$ as calculated from Harris (1996, 2010) catalogue. M31 properties: M_{200} from Villanueva-Domingo et al. (2023), $M_\star$ from Sick et al. (2015), and $M_{\rm GCs}$ as calculated from Caldwell & Romanowsky (2016) catalogue.

3.2. Globular clusters selection

The described formation and evolution model corresponds to SCs in general. To turn our attention to GCs specifically, we need to perform a physically motivated candidates selection. Recalling GCs as the products of long term evolution and survival of SCs that escaped disruptive environments and now populate the bulge and halo of galaxies, we can restrict our GC selection to SCs with kinematic signatures resulting in a spheroidal spatial distribution.

For this, we perform a kinematic decomposition through a Gaussian Mixture Model fit for a two component (spheroidal and disc) system over a three dimensional space defined by the circularity parameter[9], ϵ, orbital energy, E, and logarithm of the

[9] In this case, the circularity parameter is defined as the z-component of the angular momentum over the maximum angular momentum allowed for the orbital energy of the star particle, $\epsilon = L_z/L_{z,\max}(E)$, such that

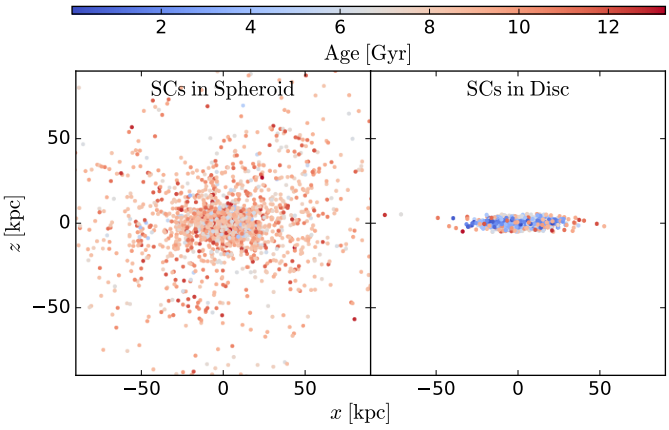


Fig. 2: Spatial distribution of the modeled SCs in the halo 6 color coded by their age in spheroidal and disc kinematic components. *Left*: SCs identified to be in the spheroidal, i.e. bulge and halo, component. *Right*: SCs identified to be in the disc component. SCs compatible with old GCs are generally scattered around the bulge and halo while younger SCs are generally concentrated towards the disc.

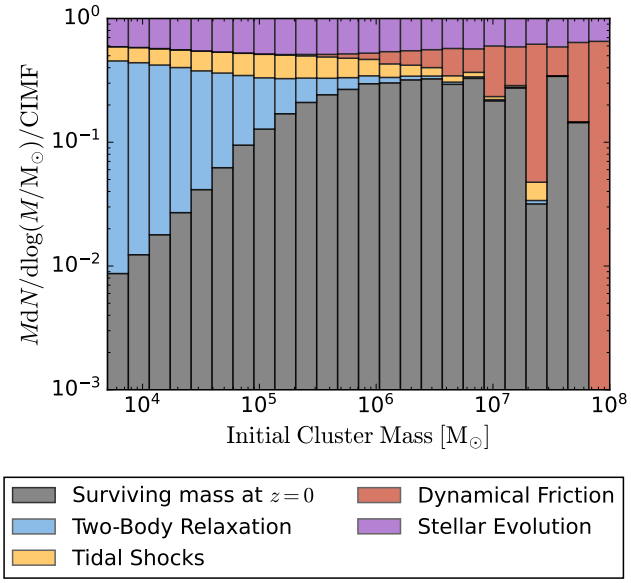


Fig. 3: Relative importance of two-body relaxation, tidal shocks, and dynamical friction disruption processes in the transformation from the CIMF to the evolved SC MF. We show the total surviving mass and mass lost by each process in each bin in initial SC mass, normalized by the CIMF.

height coordinate of the star particles, $\log|z|$. We plot the spatial distribution resulting from the decomposition in fig. 2. The distribution corresponds to the simulated SCs of halo 6 at redshift $z = 0$ and is color coded by age. We show in the left and right panels the SCs corresponding to the spheroidal and disc components, respectively. The SCs located in the disc component (right panel in fig. 2) are generally young, consistent with the observed distribution of YSCs and open clusters. In contrast, the spheroidal components (left panel in fig. 2) host SCs with generally older ages, in line with GCs being located mainly in the bulges and halos of galaxies.

Finally, we further constrain our selection to SCs with current masses $m > 10^4\,M_\odot$, well below completeness limits of extragalactic studies (Jordán et al. 2007), and comparable to the MW and M31 GCMFs completeness limit (Harris 1996, 2010; Caldwell & Romanowsky 2016). This limit also restricts our selection to SCs less affected by a potential underestimation of their tidal shocks disruption.

4. Simulated star clusters in AuriGLOBES

In the following subsections, we describe the general properties of our simulated SC populations and the effect of the different model choices.

4.1. Mass Functions under different model variations

As a first step, we explore the effect of modifying the cluster formation and evolution model. It is instructive to first see the relative importance of each of the disruption mechanisms when transforming the CIMF into the evolved SC MF in our model. We show this in fig. 3, where we plot the fraction of cluster mass lost via different mechanisms for each initial cluster mass bin. The relative importance of each mechanism is mass dependent: two-body relaxation is the main disruption mechanism for low initial SC masses ($m_0 < 10^5\,M_\odot$), while dynamical friction is the major disruption mechanism at the high mass end ($m_0 \gtrsim 10^6\,M_\odot$). Tidal shocks and two-body relaxation play a comparable role in the $10^5 < m_0/M_\odot < 10^6$ mass range. This validation mainly demonstrates that, in our model, the main disruption processes are two-body relaxation and dynamical friction. Tidal shocks have a similar, less important, disruption contribution at most scales.

We now move to compare the evolved MFs of the simulated SCs for the first four model variations of halo 6 and show them in fig. 4. For comparison, the GCMFs for the MW and M31 are included (as obtained from Harris 1996, 2010; Caldwell & Romanowsky 2016).

We first describe the behavior of the MFs of our `Fiducial` model (leftmost panel) which includes both the formation constraint to tidally compressive environments and the enhanced mass loss due to compact object heating. Although the MFs have their peak around an order of magnitude lower than the observational GCMFs (at $10^4\,M_\odot$, coinciding with our lower mass cut for the GC selection) and they retain an extended tail towards lower masses, they are consistent with a transformation of an initial Schechter CIMF into a lognomal shaped GCMF, as expected from the long-term evolution of SCs (also demonstrated by Elmegreen & Hunter 2010; Pfeffer et al. 2018; Reina-Campos et al. 2022a). In addition, the simulated GCMFs are consistent with the observed ones for masses above $10^5\,M_\odot$, especially for the $\tau > 8$ Gyr age cut, which matches the M31 GCMF. This behavior highlights the importance of combining both internal and external cluster evolution processes when modeling the long-term evolution of cluster populations.

To assess the role of each ingredient in shaping the MF, we progressively remove elements of the fiducial model. The effect of removing the compact object heating correction on the two-body relaxation mass loss can be seen in the center-left panel (`No BH heating` model). Here, the long-term evolution of the cluster population becomes significantly less efficient in removing low-mass clusters. As a consequence, the modeled MFs retain a prominent population of evolved low-mass SCs and the

circular orbits in the direction of galactic rotation have $\epsilon = 1$, counter-rotating orbits have $\epsilon < 0$, and non-circular orbits have $\epsilon \sim 0$.

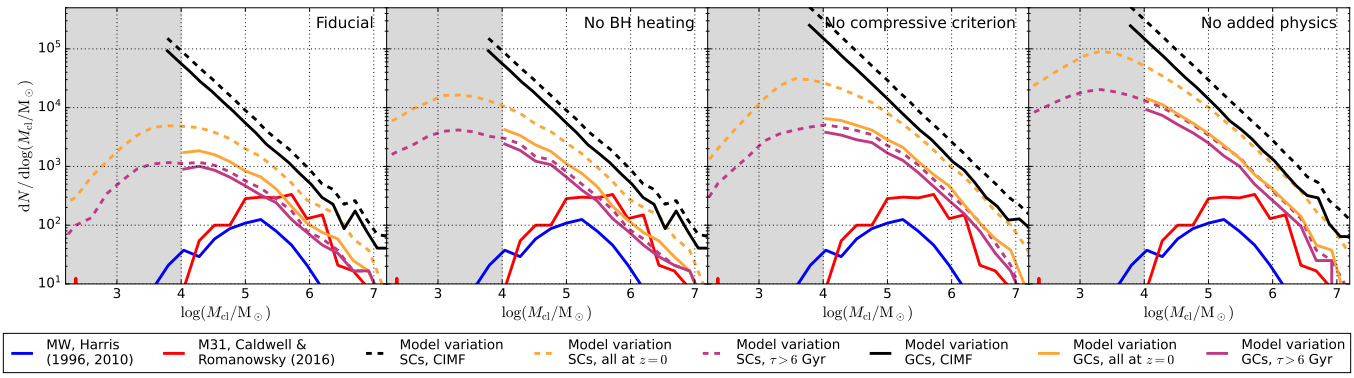


Fig. 4: Halo 6 cluster mass functions for the variations of the star cluster model choices (see table 1). From *left* to *right*, the cluster mass functions for: `Fiducial` model with all the physics described in section 2.2, `No BH heating` variation of the SCs evolution, `No compressive criterion` variation of the SCs formation, and the `No added physics` base model. The MFs for all SCs and for the GC selection (see section 3.2) are included for all the model variations, as well as the CIMFs. For comparison, the observed GCMFs from the MW and M31 are included (as obtained from Harris 1996, 2010; Caldwell & Romanowsky 2016). The shaded region in all the panels denotes the SC mass range that is excluded in our GC selection.

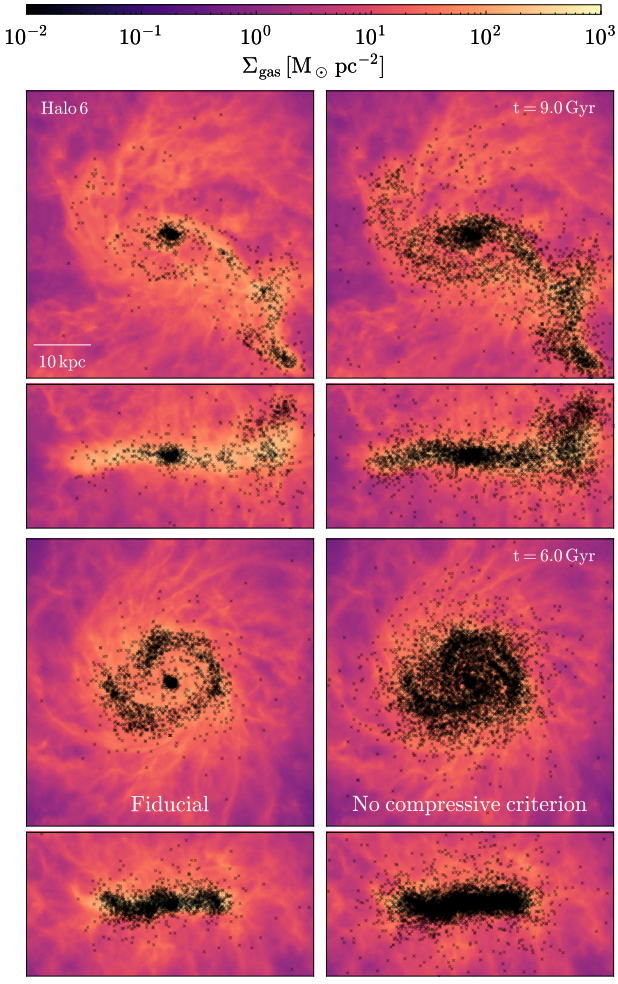


Fig. 5: Face-on and edge-on gas surface density projections of halo 6 at 9 Gyr (*top*) and 6 Gyr (*bottom*) of lookback time for two different model choices for SCs formation. The location of newly formed SCs, i.e. $\tau \lesssim 200$ Myr, is highlighted with black crosses. *Left:* `Fiducial` model with SCs forming only in tidally compressive gas. *Right:* `No compressive criterion` where SCs formation is not constrained to these environments only.

peak of the distribution shifts toward lower masses compared to the `Fiducial` case. This behavior is similar to the MF reported in E-MOSAICS (figs. 16 and 17 in Pfeffer et al. 2018). This demonstrates that enhanced mass loss driven by the retained compact object population can play a significant role in accelerating cluster evaporation and shaping the evolved MF (as in Gieles & Gnedin 2023).

If, instead, the constraint to form SCs only in tidally compressive environments is removed (`No compressive criterion`, center-right panel), there is a substantial increase in the number of clusters formed. Consequently, the normalization of both initial and evolved MFs is higher in comparison to the `Fiducial` model and the evolved MFs exceed the observations at all cluster masses, even for our GC selection at the old age cut. The peak of the old SCs MF is similar to the `Fiducial` case although it is at lower masses in the case of all the SCs at $z = 0$.

Finally, when both ingredients are removed (`No added physics`, rightmost panel), the model reverts to a simpler prescription for cluster formation and evolution, similar to E-MOSAICS but with the different choice for the initial half-mass radius and its evolution. In this case, the MFs again lie well above the observed GCMFs at all masses and the peak is nearly two orders of magnitude below the observed one.

The excessive number of clusters formed in the last two scenarios suggests that, in the absence of additional physical constraints, the model allows SCs to form in regions not favorable for their bound system nature. In particular, tidally compressive gas environments are known to favor the formation of gravitationally bound clusters (Renaud et al. 2014, 2015). We further illustrate the impact of enforcing this condition in fig. 5, where we plot the gas surface density and the location of the newly formed SCs ($\tau \lesssim 200$ Myr) at two evolutionary epochs of halo 6. These, around 9 and 6 Gyr of lookback time, correspond to two episodes of sustained high star formation, with the $t = 9$ Gyr being merger induced. We show this for the `Fiducial` model (left column) and the `No compressive criterion` variation (right column). Although the number of formed clusters for the `Fiducial` model is significantly smaller, the formation constraint ensures that it happens in high density gas regions, e.g. central region and spiral arms. For the `No compressive criterion` variation, cluster formation is widespread throughout the galaxy, hap-

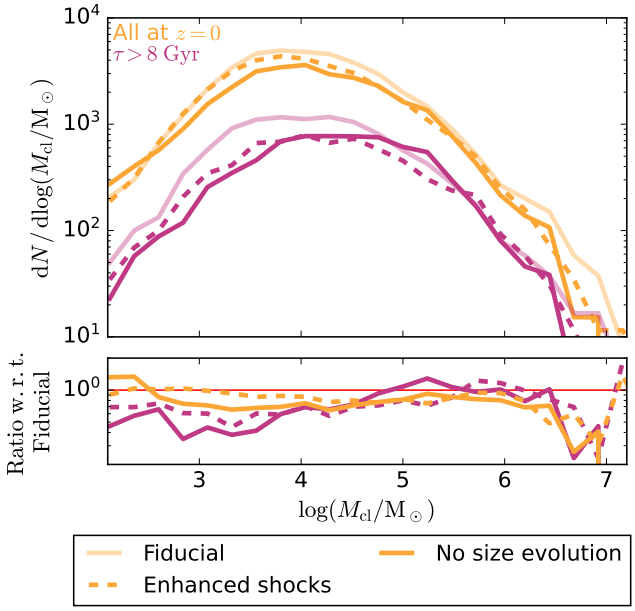


Fig. 6: *Top*: Halo 6 all SCs MFs for the `Enhanced shocks` (boosting tidal shocks by a factor of 10) and for the `No size evolution` (without evolving the clusters half-mass radius) variations in comparison to the `Fiducial` model (see table 1). The colors correspond to MFs at different age cuts, as described in the top left corner of the figure. *Bottom:* ratio of the MFs with respect to the correspondent MF from the `Fiducial` model.

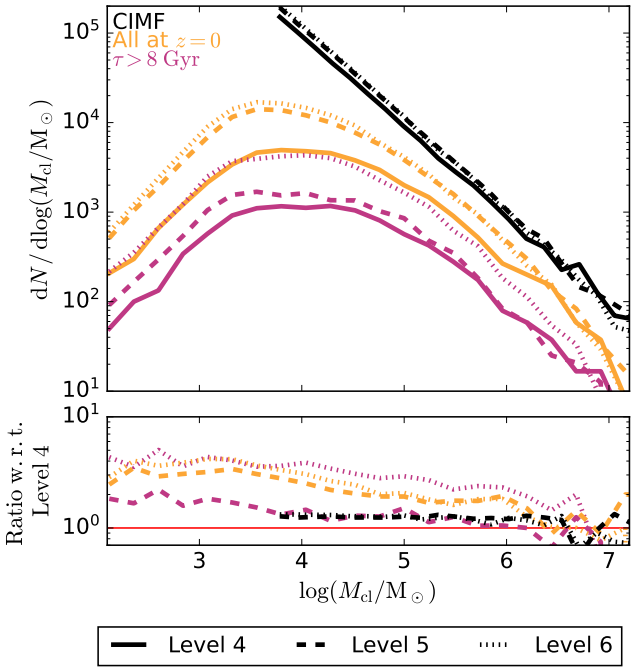


Fig. 7: *Top*: Halo 6 all SCs MFs for the fiducial run at three resolution levels: "level 4", "level 5", and "level 6". The colors correspond to MFs at different age cuts, as described in the top left corner of the figure. *Bottom:* ratio of the MFs with respect to the correspondent MF at "level 4".

pening also in low surface density regions. Consequently, ensuring a compressive environment for SCs formation reduces their overall formation rate and brings the normalization of the MFs closer to the observational constraints in fig. 4. Taken together, these comparisons indicate that both the environmental regulation of cluster formation through the implementation of the tidally compressive criterion and the enhanced dynamical mass loss associated with compact object remnants play an important role in reproducing the observed properties of GC systems in our model.

We now move to the last two variations, i.e. `Enhanced shocks` and `No size evolution`, and present their MFs in fig. 6 comparing them to those of the `Fiducial` model. With the `Enhanced shocks` variation we aim to see the effect of more disruptive shocks that could be generated from the inclusion of a more sophisticated treatment of the ISM, given that tidal shocks disruption play a minor role in our model. The effect of boosting the tidal shocks mass loss by 10 is evidenced in lowering the normalization of the MFs in fig. 6. The peak of the MFs, however, remains at the same location as that of the `Fiducial` model and the old SCs MF retains the extended tail towards low masses. We tested a higher boost factor and the behavior is a further decrease in normalization but with the same extended tail to low masses (see appendix D).

Finally, we check the effect of not including the half-mass radius evolution model, i.e. eq. 22, on the SCs disruption and we also compare the produced MFs in fig. 6. Interestingly, disruption becomes more efficient with a higher depletion at the low mass tail of the MFs, the GCMF has a similar normalization as the `Enhanced shocks` variation but the peak is shifted to $\approx 5 \times 10^4$ M$_\odot$. This result is in agreement with Gieles & Renaud (2016) and Reina-Campos et al. (2023) stating that the competition between expansion from two-body relaxation and shrinking from tidal shocks leads to an equilibrium MRR where SCs have a higher resilience to tidal disruption. With no size evolution, disruption is more effective, leading to an old SCs MF more similar to observations, in agreement with the results of Reina-Campos et al. (2022a). In our case, this is driven by the combined effect of the enhanced mass loss from two-body relaxation and the external environmental disruption.

4.2. Numerical Convergence of the Mass Functions

We now assess the numerical convergence of our `Fiducial` model by comparing the cluster MFs of halo 6 across three different resolutions: the fiducial resolution "level 4", and two lower resolutions "level 5" and "level 6" with baryonic mass resolution of $\sim 4 \times 10^5$ M$_\odot$ and $\sim 4 \times 10^6$ M$_\odot$, respectively. We present the MFs of all SCs at each resolution in the top panel of fig. 7, while in the lower panel we show the ratio of "level 5" and "level 6" MFs with respect to those of "level 4". The CIMFs for the three simulations are nearly identical across resolutions. This is partially an effect of the tidally compressive formation constraint making the cluster formation histories comparable across the three resolutions, even though their star formation histories are markedly different (behavior across resolutions explained in Grand et al. 2021; Pakmor et al. 2025a).

The evolved MFs show differences across resolution that cannot be explained by the differences in the CIMF, given that the latter shows negligible change. Instead, they show an interesting systematic trend: as resolution increases, tidal shocks disruption becomes more effective which leads to further depletion of the low mass tail of the MFs. Furthermore, the peak appears to slightly shift to higher masses as resolution increases, again owing to more effective disruption of evolved clusters at higher resolution. Finally, the MFs for the $\tau > 8$ Gyr cut in fig. 7 show

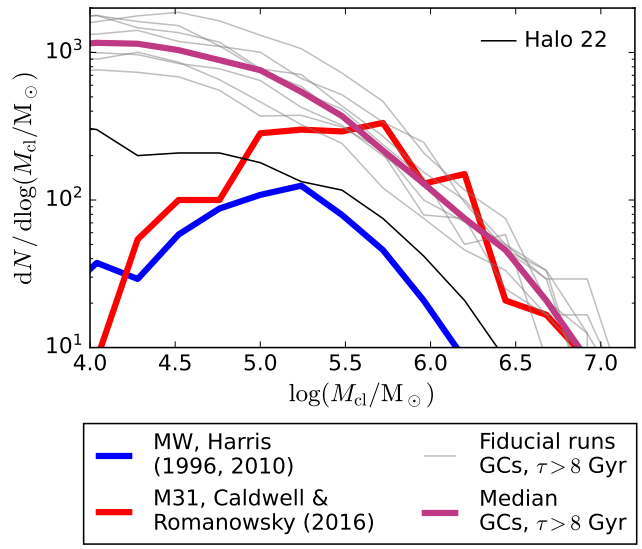


Fig. 8: GCMFs for the `Fiducial` model of the 9 rerun halos, and their median GCMF, at the $\tau = 8$ Gyr age cut. As in fig. 4, the observed GCMFs for the MW and M31 are included for comparison. The halo with the most similar GCMF to the MW for this age cut is highlighted with black continuous line.

a convergent behavior at the "level 4" and "level 5" resolutions, with the larger differences being below the $m > 10^4\,\mathrm{M}_\odot$ mass cut selection for our GC candidates. This effect is driven by an increased ability to capture tidal shocks and a deeper galaxy potential which act to enhance SC disruption.

4.3. Fiducial Globular Cluster Mass Functions

Having motivated our `Fiducial` model choice, we now present the GCMFs corresponding to the $\tau > 8$ Gyr age cut of all the re-simulated halos in fig. 8. We also show the corresponding median GCMF. There is a consistent general behavior for the GCMFs for their shape and peak location. Their differences primarily arise from the inherent normalization coming from the differences in stellar mass and star formation histories (SFHs) between the systems (see section. 4.4). The median GCMF is compatible with observational constrains for masses above $10^5\,\mathrm{M}_\odot$ and showing more similarity with M31 than with the MW population. This is explained as the median age for the observed GCs in the MW is older, i.e. $\approx$ 12 Gyr (Kruijssen et al. 2019b), than that of M31, i.e. $\approx$ 10.7 Gyr (Usher et al. 2024). Finally, we highlight the GCMF of halo 22 as the most similar to that of the MW. In particular, this halo was identified by Fattahi et al. (2019) as one of the MW-analogue halos with signatures of an early accretion event similar to the Gaia-Enceladus-Sausage (GES) merger for the MW (Belokurov et al. 2018; Helmi et al. 2018). This connection is particularly relevant as early, massive accretion events are thought to contribute a significant fraction of the GC population, and to shape the age and metallicity distributions of GCs (e.g. Kruijssen et al. 2019b; Massari et al. 2019; Newton et al. 2025).

4.4. Age Distributions

To further characterize the effect of the tidally compressive formation constraint over the formation history of SCs, we plot the Cluster Formation Rate (CFR) and age distribution for all the SCs and for the GCs for the halo 6 in the `Fiducial` and `No compressive criterion` models in fig. 9. We determine the CFR by binning the initial SC (GC selection) masses by age into 175 Myr intervals. For comparison, we include the star formation rate (SFR) of halo 6, determined binning the initial stellar masses by age in the same age intervals as for the CFR. The age distribution corresponds to the sum of normal distributions at the individual cluster ages assuming a uniform age uncertainty of 0.5 Gyr, following Valenzuela et al. (2025). Note that the CFR corresponds to all the formed SCs while the age distribution lines correspond to only those surviving until redshift $z = 0$. In the case of GCs, both curves correspond to surviving populations, given our $m > 10^4\,\mathrm{M}_\odot$ selection. The age distribution of the MW GCs is also included for comparison and was constructed with the same methodology using, in this case, the available uncertainties of the estimated ages. The ages, and their uncertainties, come from the Kruijssen et al. (2019b) compilation catalogue, averaging GC ages and uncertainty estimates from different studies (Forbes & Bridges 2010; Dotter et al. 2010; Dotter et al. 2011; VandenBerg et al. 2013).

The compressive formation constraint has a big impact in inhibiting SC formation while maintaining starburst periods and following the overall SFR of the halo. The biggest impact is at low redshifts where the SC formation is heavily reduced. This turns into an age distribution favoring older populations, as seen in the lower panel of fig. 9. The same effect is visualized for the GC candidates CFR, retaining, however, mostly the same age distribution. This demonstrates that the tidally compressive constraint is successful not only in reducing SC formation but also in retaining the formation of potential GC candidates.

We also include the age distributions for all the fiducial runs in the lower panel of fig. 9. This illustrates how the variety of assembly histories for the different halos drives different age distributions of their GC populations. However, we note a qualitative mismatch between the simulated distributions and that of the MW. As seen in the lower panel, the empirical distribution is dominated by a peaked, ancient population at $t \approx 12$ Gyr, and an almost complete truncation towards surviving clusters at younger ages. In contrast, our simulated populations exhibit much broader, continuous age distributions peaking at intermediate ages ($t \approx 6-9$ Gyr). This can be partially attributed to the ICs of the simulated halos being not similar enough to the MW and its assembly history, or a consequence of the underlying Auriga galaxy formation model not matching the high SFR of the MW (Snaith et al. 2015) at very high redshift ($z > 5$), which delays the simulated peak of SC formation. However, the continuous tails towards younger surviving clusters could imply that significant physical ingredients could be missing from the sub-grid modeling of SCs. Specifically, this points to either a potential underestimation of their disruption, or insufficient suppression of their formation in recent star formation periods. This qualitative mismatch serves as an interesting constraint as it underscores that the precise assembly history of the MW provided a highly specific environment for GC formation and survival that remains challenging to replicate with current sub-grid models.

We further analyze the diversity of the halos assembly histories and their imprint on the simulated age distributions in fig. 10 where we show the lookback times at which the host galaxies assembled 25 and 50 per cent of their total stellar mass, $t_{\rm SF,25}$ and $t_{\rm SF,50}$ (top panel) and the median ages of their SCs and GCs populations in comparison to $t_{\rm SF,25}$ (bottom panel). For comparison, the corresponding timescales and median GC age for the MW and M31 systems are included. The 25 and 50 per cent of star formation timescales where calculated from the estimated

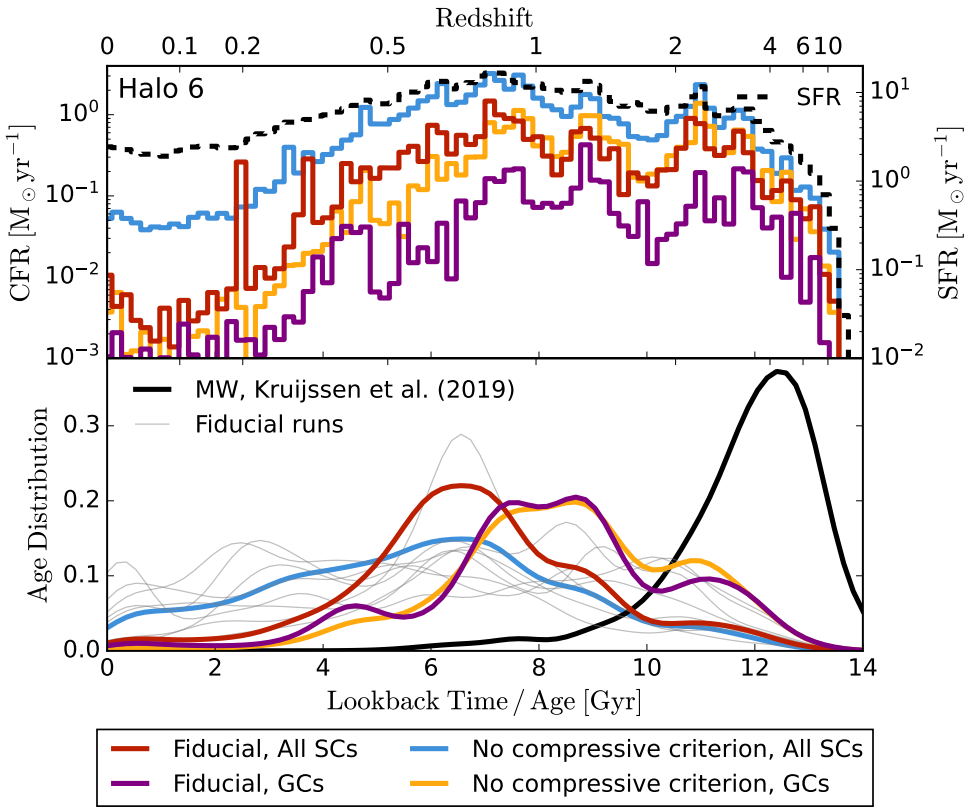


Fig. 9: *Top*: All SCs and GC selection cluster formation rate of halo 6 for the `Fiducial` and `No compressive criterion` variations. The star formation history of the halo is included for comparison. *Bottom*: Age distribution of surviving SCs and GC selection for the same model variations. The MW GCs age distribution is included for comparison, corresponding to the average GCs ages and uncertainties compiled by Kruijssen et al. (2019b). Included too are the age distributions for all the rerun halos (thin gray lines), exemplifying the variability of cluster age distributions from halo to halo. The tidal formation constraint heavily impacts the formation rate of SCs while retaining the age distribution of the GC selection.

SFHs in Snaith et al. (2015) for the MW and in Williams et al. (2017) for M31. The GC system median age for the MW is calculated from Kruijssen et al. (2019b) catalogue while the median age for M31 is the value quoted in table 2 of Usher et al. (2024). Markedly, both the MW and M31 form 25 and 50 per cent of their stellar mass very early on: $t > 12$ Gyr of lookback time for the 25 per cent, and $t > 10$ Gyr for the 50 percent; with the MW having formed 50 percent of its stellar mass earlier than M31. In contrast, all of the simulated halos have these timescales much later: the halo with earliest star formation, halo 23, forms 25 and 50 per cent of its stellar mass at $t \approx 10$ and $t \approx 7.5$ Gyr of lookback time, respectively. The median timescales for the simulated halos are $t \approx 9.22$ and $t \approx 6.75$ Gyr of lookback time. These quantities trace the early assembly history of the galaxies allowing us to assess how the cluster formation relates to the global buildup of stellar mass.

In the lower panel of fig. 10 we show the median ages for all the SCs surviving at $z = 0$ in circled markers, for the GC selection in diamond markers, and for the GC selection plus a metallicity cut of [Fe/H] < -0.5 dex in down-facing triangle markers. With this metallicity cut we aim to target the old population of our GC selection. There is an evident trend across the three selections such that galaxies that assemble their stellar mass earlier tend to host older SC and GC populations, albeit with some scatter. This scatter is driven by the continued formation of clusters at later times and is diminished when targeting the older populations with the metallicity cut. The MW and M31 GC systems, with median ages of $\approx$ 12 Gyr and $\approx$ 10.7 Gyr, respectively, confirm this trend. Therefore, this shows that a high SFR at the earliest stages of galaxy assembly is needed in order to obtain GC age distributions comparable to that of the MW or M31. We highlight again halo 22 here with bigger markers: it is one of the halos with an old GC population (after the metallicity cut) with median age close to the observed median age of MW. This is despite having a lower rate of star formation to the one of the MW, specially in the first 2–3 Gyr of evolution. Furthermore, the GC median age following this cut approximately coincides with the GES analogue merger of the halo. We show an extended comparison of the individual halos SFHs with their SC age distributions with respect to the MW in appendix E. Overall, these results support the interpretation that GCs predominantly trace the early SFH of their host galaxies.

4.5. Metallicity Distributions

Tied to the age distribution of the GCs is their metallicity distribution. In fig. 11 we show the individual metallicity distribution functions (MDF) of the fiducial runs at the $\tau > 8$ Gyr age cut, as well as the median simulated distribution. The GCs metallicities, [Fe/H], correspond to the metallicity of their par-

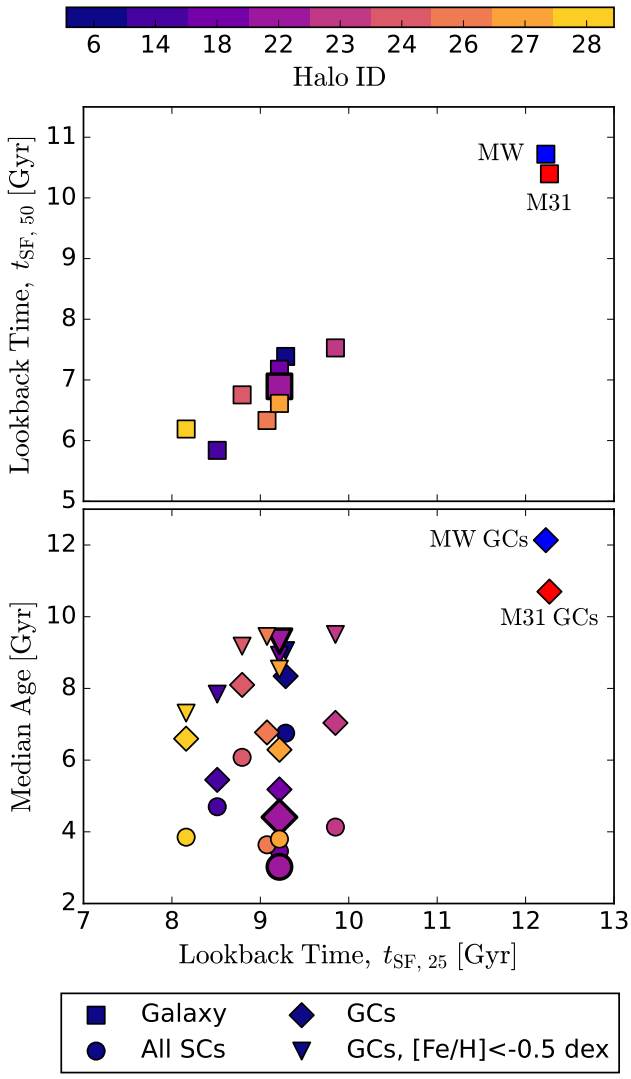


Fig. 10: Individual galaxy stellar mass assembly characteristic timescales and their SCs (GCs) population median age. *Top*: timescale for each galaxy to form 25 and 50 per cent of its total stellar mass. The timescales for the MW and M31 are included for comparison as calculated from their estimated SFH in Snaith et al. (2015) and Williams et al. (2017), respectively. *Bottom*: median age of their SC/GC system in comparison to the timescale for forming 25 per cent of their total stellar mass. The GC median age for the MW GC system is calculated from Kruijssen et al. (2019b) while the median age for the M31 GC system is the value quoted in table 2 of Usher et al. (2024). Halo 22, and its SCs/GCs populations, are highlighted with a larger size marker.

ent star particle[10]. The MDFs from the MW and M31 GC populations are included in the figure for comparison (as extracted from Harris 1996, 2010; Caldwell & Romanowsky 2016). The simulated MDFs have a general trend of being richer in metallicity compared to the MW. However, comparing to the M31 MDF, we can see that the simulated MDFs cover the same metallicity

[10] We apply a correction offset of −0.5 dex following Grand et al. (2021) showing that Auriga galaxies are too metal rich relative to the observed stellar mass – stellar metallicity relation (e.g. Kirby et al. 2013)

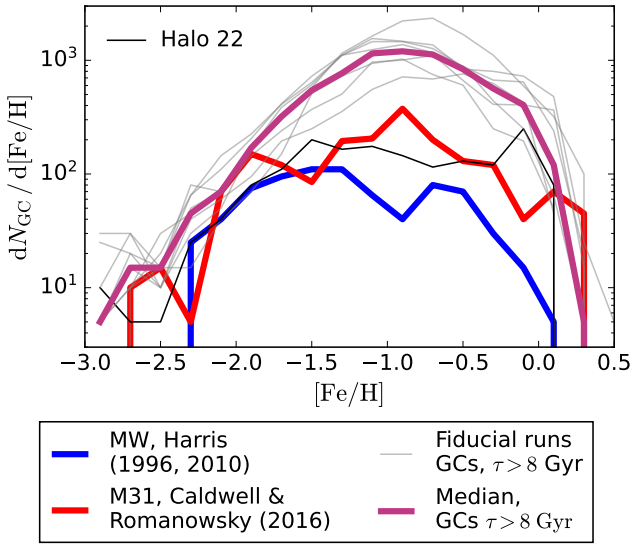


Fig. 11: Metallicity distribution functions of the old ($\tau > 8$ Gyr) population of GCs of the fiducial runs, and their median distribution, compared to the MW and M31 MDFs (extracted from Harris 1996, 2010; Caldwell & Romanowsky 2016). The halo with the most similar MDF to the MW for this age cut is highlighted with black continuous line.

range, albeit with a higher number of GCs in the −1.75 to 0.3 [Fe/H] range.

Similar to the lower panel of fig. 9 (see also fig. E.1), the diversity of MDFs in fig. 11 is a result of the different assembly histories of the simulated halos. Therefore, the median MDFs illustrate that the simulated clusters are more metal rich because they are generally formed at later times compared to the MW and M31. Below [Fe/H] ≈ −1.75, all the simulated MDFs and their medians agree well with the MW and M31 MDFs and none of them show an important population below the "metallicity floor" of [Fe/H] = −2.5 (Beasley et al. 2019; Kruijssen 2019). We note again that halo 22 gives the MDF most similar to that of the MW. Furthermore, it shows signatures of bimodality, albeit with a dip at a slightly higher metallicity of [Fe/H] ≈ −0.7. Overall, the simulated GC age and metallicity diversity highlight that GCs remain sensitive probes of galactic assembly.

4.6. Spatial Distribution

In this section, we consider the spatial distribution properties of our simulated populations. As illustrated in fig. 2, SCs consistent with younger populations are generally distributed along the disc component of the galaxies while older populations populate the dispersed spheroidal component, i.e. a bulge/halo. While the SCs distribution in fig. 2 is from halo 6 only, all the simulations summarized in table 2 have a similar behavior with a median age difference for the SCs in both components of ≈ 2 Gyr on average (see also fig. 10).

Focusing now in the spatial distribution of our GCs selection only, we show in fig. 12 the number density radial profile of all the halos with the fiducial model in comparison to the profile of the MW GCs (based on the distance estimates in Harris 1996, 2010). The simulated GCs follow a similar profile across the galaxy with the difference in the normalization reflecting the different stellar masses for the different halos. The median profile for the $\tau > 8$ Gyr age cut is a factor of a few higher than the MW

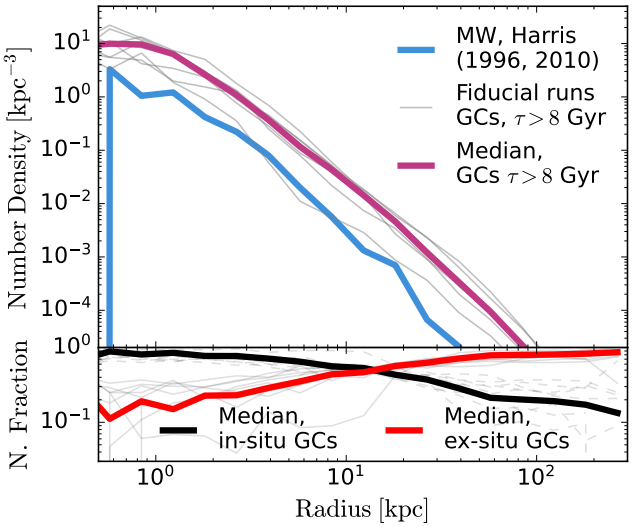


Fig. 12: *Top:* Number density radial profile of the old ($\tau > 8$ Gyr) simulated GCs of the `Fiducial` runs, in gray, in comparison to the distribution of GCs in the MW. *Bottom:* Fraction of in-situ (dashed gray lines) and ex-situ (continuous gray lines) GC candidates at the same age cut as a function of the galactocentric radius.

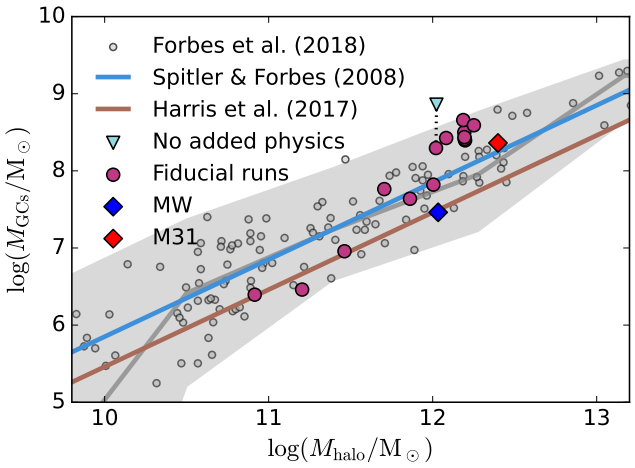


Fig. 13: GC system mass – halo mass relation for the simulated halos. Included are: the compilation of galaxies across different masses and morphologies presented in Forbes et al. (2018), and the MW and M31 systems from the values quoted in table 2. The gray continuous line is the median and the shaded region is the 2σ of the distribution of the galaxies in Forbes et al. (2018). Also included are the empirical relations derived by Spitler & Forbes (2009); Harris et al. (2017). For the `Fiducial` model, the simulated GC systems masses, according to the GC candidate selection and old ages ($\tau > 8$ Gyr), generally lie inside the observed scatter of the empirical relation. The `No added physics` variation of halo 6, on the other hand, gives a total mass in old GCs that sits above the observational scatter and almost an order of magnitude higher than the `Fiducial` model.

profile with a consistent slope. Additionally, in the bottom panel of fig. 12 we include the distribution of in-situ and ex-situ GCs in the simulated populations quantified by their number fraction as a function of radial distance from the galactic centre. In-situ GCs are primarily in the inner regions while ex-situ GCs are located in the outer halo regions. However, there are both ex-situ GCs at small radii, e.g. $R_{\rm GC} < 10$ kpc, and in-situ GCs at high radii, e.g. $R_{\rm GC} > 30$ kpc (behavior also identified in e.g. Pfeffer et al. 2020; Reina-Campos et al. 2022b; Chen & Gnedin 2024b).

4.7. GC system mass – halo mass relation

Finally, we examine the GC system mass – halo mass relation first introduced in Spitler & Forbes (2009) for our `Fiducial` simulations. To probe a wider mass range than 1–2 $\times 10^{12}$ M$_\odot$ for the MW and M31, we expand our simulation suite by adding 5 lower mass halos. These are the halos L1 and L10 in the 5×10^{11} M$_\odot$ $< M_{200}(z = 0) < 10^{12}$ M$_\odot$ mass range (table 3, `LowMassMWs` in Grand et al. 2024) and halos 4, 7 and 10 in the 5×10^{10} M$_\odot$ $< M_{200}(z = 0) < 5 \times 10^{11}$ M$_\odot$ mass range (table 4, `Halos_1e11msol` in Grand et al. 2024). We show the total mass in GCs for the extended `Fiducial` runs in the GC system mass – halo mass plane in fig. 13. The simulated halos cover a total dynamical mass range of 8×10^{10} to 2×10^{12} M$_\odot$ and the total GC system mass is calculated from the total mass of our GC selection with ages $\tau > 8$ Gyr. Included in fig. 13 are two different fits of the empirical relations presented in Spitler & Forbes (2009) and Harris et al. (2017), and the compilation of systems across different morphologies and masses presented in Forbes et al. (2018). The gray continuous line and the shaded region correspond to the median and 2σ-region of the distribution of these systems, respectively. We also include the position of the MW and M31 for the values quoted in table 2. Lastly, the `No added physics` model of the halo 6 is also included. The GC system mass from this `No added physics` model sits well above the 2σ region of the expected total GCs mass for its halo mass, while the total GC system mass for the `Fiducial` run is inside this scatter. This gives further support for constraining GC formation to fully compressive gas regions for a more realistic modeling of SC formation, and the inclusion of compact object heating. Looking at all the simulated GC populations, they all lie inside the observed scatter of the empirical relation. The trend, however, seems to follow a steeper relation across the simulated mass range. This suggests that a wider study with more simulated halos is needed to constrain the drivers of the slope of the simulated relation. Overall, this picture demonstrates that the fiducial model is able to produce reasonable total GC system masses across a range of halo masses, given the physically motivated candidate selection.

5. Discussion

Our simulated GC populations can be directly compared to those of the aforementioned E-MOSAICS (Pfeffer et al. 2018; Kruijssen et al. 2019a) and EMP-Pathfinder (Reina-Campos et al. 2022a, 2023) projects, owing to similarities of the subgrid models. Despite differences in both the underlying galaxy formation and the subgrid cluster models, these simulations manage to reproduce the high mass end of the observed GCMF. By matching their published MFs against our suite of simulations (comparison performed in fig. 14), we discuss here how different assumptions of star formation and SCs mass loss affect the simulated population of SCs. We first note that, even though the three projects implement the same CFE model (Kruijssen 2012), we needed to further constrain SCs formation in order to match the high mass end of the GCMF. This is a consequence of the different galaxy formation models as follows:

EAGLE (Crain et al. 2015; Schaye et al. 2015), the base model for E-MOSAICS, implements a star formation prescription that is a function of the gas pressure (Schaye & Dalla Vecchia 2008) and a metallicity dependent density threshold (Schaye 2004). In contrast, the star formation prescription in Auriga is solely a function of the gas density (Springel & Hernquist 2003). While the characteristic pressure of star-forming gas fluctuates by orders of magnitude in both models due to mergers, gas accretion rate, and feedback (e.g. see fig. 5 in Pfeffer et al. 2018), we have verified that the characteristic pressure of star forming gas in Auriga is persistently higher. Particularly, this pressure corresponds to the effective equation of state of the two phase ISM model. Given that the CFE model is a monotonic function of the pressure, the calculated CFE in Auriga remains high, i.e. $\Gamma \gtrsim 0.1$, at all times. Additionally, the Auriga galaxy formation model produces galaxies more massive in stars for the same halo mass, in comparison with EAGLE, leading to a higher mass budget for SC formation.

For EMP-Pathfinder, the galaxy formation model also gives a continuous SC formation with a high CFE across the galaxy assembly history (see fig. 12 in Reina-Campos et al. 2022a). Nevertheless, the mass budget for SCs formation is lower than in Auriga from their galaxies being less massive in stars for similar halo masses (see table 2 in Reina-Campos et al. 2022a). Particularly, the explicit multi-phase ISM model allowing gas to cool down to $T \sim 100$ K before reaching the density threshold for star formation could be playing the role of environmental regulation for star clusters formation. Additionally, the more efficient mass loss from tidal shocks contributes to their simulated MFs to match the MW GCMF across all masses.

We now move to compare the low mass end of the MFs across our simulated populations and those of E-MOSAICS and EMP-Pathfinder. In fig. 14 we show the MFs of our variations comparing well with the MFs reported in E-MOSAICS and EMP-Pathfinder. All of the MFs correspond to SCs at the $\tau > 10$ Gyr age cut. Note that the different age cut plotted here, instead of the $\tau > 8$ Gyr used in the rest of the paper, is to match the published MFs from these projects. We can see that our `No BH effect` model matches the MF from E-MOSAICS, demonstrating a consistent behavior from adopting similar assumptions. The comparison with the MFs from EMP-Pathfinder is not as straightforward: while our `Fiducial` model compares well with the "MW04_drhdt" MF reported in Reina-Campos et al. (2023) (for the same initial size prescription, albeit with more clusters in the $10^3 < m/\mathrm{M}_\odot < 10^4$ mass range), our `No size evolution` variation sits well above the "Fiducial" MF from Reina-Campos et al. (2022a) (that does not include size evolution) for masses $m < 10^5\,\mathrm{M}_\odot$. Although both models show the same behavior, the effect of not including size evolution is milder in our model.

Although the quantitative alignment between the simulation suites shows variations due to the distinct sub-grid physics, the comparisons demonstrate that different theoretical approaches can yield similarly evolved MFs. Particularly, this highlights a degree of degeneracy in the mechanisms shaping GC populations. Moreover, both simulation suites confirm that efficient mass-loss prescriptions are needed to sufficiently disrupt the evolved low-mass SCs and recover MFs consistent with observations. In our case, this is achieved through the implementation of the compact object heating correction in the two body relaxation prescription. Furthermore, both models demonstrate that incorporating the size evolution of SCs acts as an agent suppressing the effectiveness of these disruption mechanisms. More studies

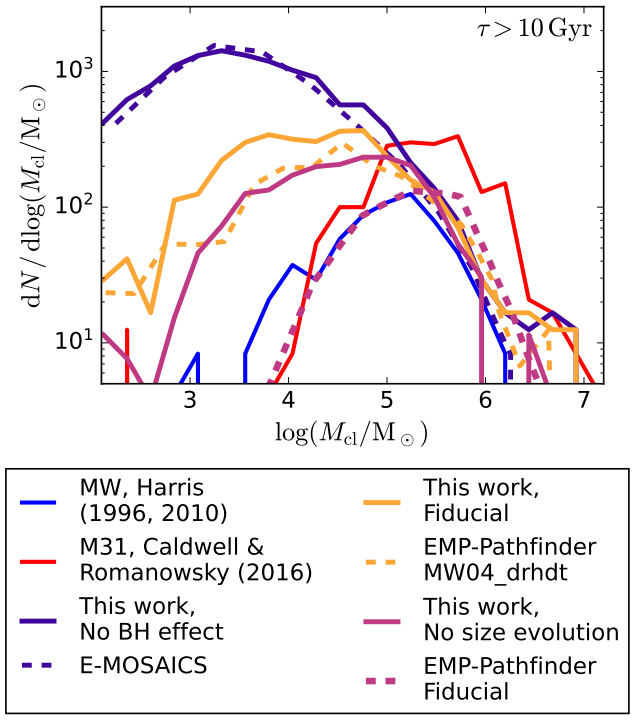


Fig. 14: Comparison of this work simulated MFs with respect to those of E-MOSAICS (Pfeffer et al. 2018; Kruijssen et al. 2019a) and EMP-Pathfinder (Reina-Campos et al. 2022a, 2023) projects. All the simulated MFs correspond to old SCs at the $\tau > 10$ Gyr age cut. Form our work, we only plot the models that compare well to the mentioned projects. For E-MOSAICS, the distribution corresponds to the median MF of 25 zoom-in MW-mass simulations plotted in fig. 8 in Reina-Campos et al. (2022a). From the same figure, we extracted the Fiducial MF of EMP-Pathfinder (with no size evolution) while the MW04_drhdt model, that includes size evolution, was extracted from fig. 4 in Reina-Campos et al. (2023).

are needed in order to characterize better this effect and improve the subgrid modelling of the size evolution of clusters.

Finally, as shown by Reina-Campos et al. (2022a), tidal shocks-driven disruption of SCs is sensitive to the treatment of the ISM in the galaxy formation model. Our `Enhanced shocks` variation aimed to mimic the effect of the inclusion of a multiphase ISM on the SCs disruption and indeed showed a more disruptive scenario but with a different behavior than in EMP-Pathfinder. Namely, the peak of the MFs is not shifted to higher masses and the MF keeps a populated low mass tail (see figs. 6 and D.1). Our test, however, is not conclusive and running AuriGLOBES with a different ISM model, e.g. SMUGGLE (Marinacci et al. 2019), could help to characterize better the effect of the cold ISM structure in our SC population. Additionally, we also note that following the behavior of the MFs in fig. 7, resolution has an effect on the ability to capture tidal shock disruption. In this sense, the underestimation of tidal shocks disruption seen in Pfeffer et al. (2018) for E-MOSAICS could partially be attributed to the resolution of the simulation suite.

To summarize, our work complements earlier findings on environmental cluster disruption mechanisms and simulated SC populations across cosmic history. All of these similar subgrid models lay the foundation to constrain GC formation and evolution in a cosmological context. Nevertheless, it is evident that

further work is needed to characterize the different processes shaping the GC population through cosmic history. Additionally, further extensions to this foundation could explore self-consistent formation pathways of different structures such as the stellar streams population arising from GC disruption.

6. Conclusions

We have introduced AuriGLOBES, a physically motivated subgrid model of SC formation and evolution inside the Auriga galaxy formation model. With our model we aim to further constrain our understanding of GC populations and how they have been shaped through cosmic time. To this end we implemented two novel approaches in the subgrid modelling of SCs: to constrain their formation to tidally compressive environments only, and to include a correction factor to account for the dynamical heating from their compact object remnants population. Our main conclusions are:

- Our `Fiducial` model produces GC populations that are in agreement with the empirical GC system mass – halo mass relation across a halo mass range of 10^{11} $M_\odot$–10^{12} $M_\odot$, and with plausible properties in terms of their spatial, metallicity, and age distributions.
- An important aspect of our model is the environmental regultaion of GC formation via tidally compressive tides. This is in addition to the gas properties, e.g. density and pressure, that are taken into account in the particular CFE calculation.
- Reproducing a GCMF consistent with observational constraints requires an effective prescription of tidal shocks disruption, two-body relaxation, and dynamical friction. In particular, we showed that two-body relaxation prescriptions should also account for the heating of compact object remnants.
- The effectiveness of tidal shocks is affected not only by the inclusion of a cold phase in the ISM model but also on the resolution of the simulation.
- In agreement with the EMP-Pathfinder simulations (Reina-Campos et al. 2022a, 2023), the size evolution of SCs suppresses the effectiveness of the disruption mechanisms.
- The diversity of the age, metallicity, and spatial distributions of our simulated GC populations reflect the variation of assembly and accretion histories of the parent halos, reinforcing the role of GCs as fossil records of galactic growth. In particular, there is a clear correlation of GC formation with early star formation in the galaxies.
- Among the simulated halos, the old GC population of halo 22 is the one with closer resemblance to that of the MW in terms of the mass, metallicity, and age distributions. In particular, this halo has been previously identified to include a GES analogue merger that could play a role shaping its GC population. We defer a dedicated analysis of the imprint of the halos assembly histories on their GC populations to future work.

Finally, we reinforce that AuriGLOBES represents a reliable framework for SC and GC population studies. Its relatively cheap overhead on top of the Auriga model makes it appealing for its application to larger cosmological volumes or statistical sample of galaxies. In addition, its AREPO-based modularity and its on-the-fly functionality open exciting avenues for further characterize the GC population and streams generated from their disruption. Namely, our future plans include generating the stellar streams with a spawning routine similar to the SUPERSTARS method in Auriga (Pakmor et al. 2025b) as well as trying other models of ISM with our AuriGLOBES framework.

Acknowledgements. We thank the referee for the comments and suggestions that helped to improve this manuscript. This work has been supported by the Spanish Ministry of Science and Innovation and Universities (MCIN/AEI/10.13039/501100011033/ - FEDER) through the research grants PID2021-122603NB-C22 and the Spanish Ministry of Science, Innovation and Universities (MICIU) PID2024-156100NB-C22. This study made use of Prospero high-performance computing facility at Liverpool John Moores University. The authors acknowledge financial support from the Royal Society under grant RGS/R2/242421. The authors thankfully acknowledge the technical expertise and assistance provided by the Spanish Supercomputing Network (Red Española de Supercomputación), as well as the computer resources used: the LaPalma Supercomputer, located at the Instituto de Astrofísica de Canarias. The authors wish to acknowledge the contribution of the IAC High-Performance Computing support team and hardware facilities to the results of this research. RJJG acknowledges support from the STFC Ernest Rutherford Fellowship (ST/W003643/1). MRC acknowledges funding from the Global Talent Junior Fellowship Programme at the Instituto Galego de Física de Altas Enerxías (IGFAE), supported by grant CEX2023-001318-M (María de Maeztu Unit of Excellence and Agencia Española de Investigación / 10.13039/501100011033). This work has received financial support from the Xunta de Galicia (CIGUS Network of Research Centres) and the European Union through the Galicia Feder 2021-2027 Program. MRC gratefully acknowledges the Canadian Institute for Theoretical Astrophysics (CITA) National Fellowship for partial support; this work was supported by the Natural Sciences and Engineering Research Council of Canada (NSERC) [funding reference number 568580].

References

Adamo, A., Bradley, L. D., Vanzella, E., et al. 2024, Nature, 632, 513
Adamo, A., Hollyhead, K., Messa, M., et al. 2020, MNRAS, 499, 3267
Adamo, A., Ryon, J. E., Messa, M., et al. 2017, ApJ, 841, 131
Alexander, P. E. R. & Gieles, M. 2012, MNRAS, 422, 3415
Alexander, P. E. R., Gieles, M., Lamers, H. J. G. L. M., & Baumgardt, H. 2014, MNRAS, 442, 1265
Andersson, E. P., Mac Low, M.-M., Agertz, O., Renaud, F., & Li, H. 2024, A&A, 681, A28
Barnard, R., Garcia, M., & Murray, S. S. 2012, ApJ, 757, 40
Barnes, J. & Hut, P. 1986, Nature, 324, 446
Bastian, N. 2008, MNRAS, 390, 759
Baumgardt, H. & Makino, J. 2003, MNRAS, 340, 227
Beasley, M. A., Leaman, R., Gallart, C., et al. 2019, MNRAS, 487, 1986
Belokurov, V., Erkal, D., Evans, N. W., Koposov, S. E., & Deason, A. J. 2018, MNRAS, 478, 611
Brodie, J. P. & Strader, J. 2006, ARA&A, 44, 193
Brown, G. & Gnedin, O. Y. 2021, MNRAS, 508, 5935
Caldwell, N. & Romanowsky, A. J. 2016, ApJ, 824, 42
Cautun, M., Benítez-Llambay, A., Deason, A. J., et al. 2020, MNRAS, 494, 4291
Chabrier, G. 2003, PASP, 115, 763
Chen, Y. & Gnedin, O. Y. 2024a, MNRAS, 527, 3692
Chen, Y. & Gnedin, O. Y. 2024b, The Open Journal of Astrophysics, 7, 23
Claeyssens, A., Adamo, A., Kokorev, V., et al. 2026, arXiv e-prints, arXiv:2601.16281
Claeyssens, A., Adamo, A., Messa, M., et al. 2025, MNRAS, 537, 2535
Crain, R. A., Schaye, J., Bower, R. G., et al. 2015, MNRAS, 450, 1937
Creasey, P., Sales, L. V., Peng, E. W., & Sameie, O. 2019, MNRAS, 482, 219
De Lucia, G., Kruijssen, J. M. D., Trujillo-Gomez, S., Hirschmann, M., & Xie, L. 2024, MNRAS, 530, 2760
Della Croce, A., Aros, F. I., Vesperini, E., et al. 2024, A&A, 690, A179
Deng, Y., Li, H., Liu, B., et al. 2024, A&A, 691, A231
Dickson, N., Smith, P. J., Hénault-Brunet, V., Gieles, M., & Baumgardt, H. 2024, MNRAS, 529, 331
Dornan, V. & Harris, W. E. 2025, ApJ, 988, 70
Dotter, A., Sarajedini, A., & Anderson, J. 2011, ApJ, 738, 74
Dotter, A., Sarajedini, A., Anderson, J., et al. 2010, ApJ, 708, 698
Duerr, R., Imhoff, C. L., & Lada, C. J. 1982, ApJ, 261, 135
Ekström, S., Georgy, C., Eggenberger, P., et al. 2012, A&A, 537, A146
Elmegreen, B. G. 2002, ApJ, 577, 206
Elmegreen, B. G. & Efremov, Y. N. 1997, ApJ, 480, 235
Elmegreen, B. G. & Hunter, D. A. 2010, ApJ, 712, 604
Fall, S. M. & Zhang, Q. 2001, ApJ, 561, 751
Fattahi, A., Belokurov, V., Deason, A. J., et al. 2019, MNRAS, 484, 4471
Faucher-Giguère, C.-A., Lidz, A., Zaldarriaga, M., & Hernquist, L. 2009, ApJ, 703, 1416
Forbes, D. A. & Bridges, T. 2010, MNRAS, 404, 1203
Forbes, D. A. & Gannon, J. S. 2025, MNRAS, 543, L1

Forbes, D. A., Read, J. I., Gieles, M., & Collins, M. L. M. 2018, MNRAS, 481, 5592
Genel, S., Vogelsberger, M., Nelson, D., et al. 2013, MNRAS, 435, 1426
Gieles, M., Alexander, P. E. R., Lamers, H. J. G. L. M., & Baumgardt, H. 2014, MNRAS, 437, 916
Gieles, M. & Gnedin, O. Y. 2023, MNRAS, 522, 5340
Gieles, M., Heggie, D. C., & Zhao, H. 2011, MNRAS, 413, 2509
Gieles, M., Portegies Zwart, S. F., Baumgardt, H., et al. 2006, MNRAS, 371, 793
Gieles, M. & Renaud, F. 2016, MNRAS, 463, L103
Giersz, M. & Heggie, D. C. 1994, MNRAS, 268, 257
Giesers, B., Dreizler, S., Husser, T.-O., et al. 2018, MNRAS, 475, L15
Gnedin, O. Y., Hernquist, L., & Ostriker, J. P. 1999a, ApJ, 514, 109
Gnedin, O. Y., Lee, H. M., & Ostriker, J. P. 1999b, ApJ, 522, 935
Gnedin, O. Y. & Ostriker, J. P. 1997, ApJ, 474, 223
Grand, R. J. J., Fragkoudi, F., Gómez, F. A., et al. 2024, MNRAS, 532, 1814
Grand, R. J. J., Gómez, F. A., Marinacci, F., et al. 2017, MNRAS, 467, 179
Grand, R. J. J., Marinacci, F., Pakmor, R., et al. 2021, MNRAS, 507, 4953
Grisdale, K., Agertz, O., Renaud, F., et al. 2019, MNRAS, 486, 5482
Grudić, M. Y. & Hopkins, P. F. 2020, MNRAS, 495, 4306
Gutcke, T. A. 2024, ApJ, 971, 103
Halbesma, T. L. R., Grand, R. J. J., Gómez, F. A., et al. 2020, MNRAS, 496, 638
Harris, W. E. 1991, ARA&A, 29, 543
Harris, W. E. 1996, AJ, 112, 1487
Harris, W. E. 2010, arXiv e-prints, arXiv:1012.3224
Harris, W. E., Blakeslee, J. P., & Harris, G. L. H. 2017, ApJ, 836, 67
Harris, W. E. & Pudritz, R. E. 1994, ApJ, 429, 177
Helmi, A., Babusiaux, C., Koppelman, H. H., et al. 2018, Nature, 563, 85
Hénon, M. 1961, Annales d'Astrophysique, 24, 369
Hénon, M. 1965, Annales d'Astrophysique, 28, 992
Holtzman, J. A., Faber, S. M., Shaya, E. J., et al. 1992, AJ, 103, 691
Ibata, R. A., Gilmore, G., & Irwin, M. J. 1994, Nature, 370, 194
Jenkins, A. 2013, MNRAS, 434, 2094
Johnson, K. E., Leroy, A. K., Indebetouw, R., et al. 2015, ApJ, 806, 35
Johnson, L. C., Seth, A. C., Dalcanton, J. J., et al. 2017, ApJ, 839, 78
Jordán, A., McLaughlin, D. E., Côté, P., et al. 2007, ApJS, 171, 101
Keller, B. W., Wadsley, J. W., Wang, L., & Kruijssen, J. M. D. 2019, MNRAS, 482, 2244
Kim, J.-h., Ma, X., Grudić, M. Y., et al. 2018, MNRAS, 474, 4232
King, I. 1962, AJ, 67, 471
Kirby, E. N., Cohen, J. G., Guhathakurta, P., et al. 2013, ApJ, 779, 102
Kremer, K., Ye, C. S., Rui, N. Z., et al. 2020, ApJS, 247, 48
Kruijssen, J. M. D. 2009, A&A, 507, 1409
Kruijssen, J. M. D. 2012, MNRAS, 426, 3008
Kruijssen, J. M. D. 2014, Classical and Quantum Gravity, 31, 244006
Kruijssen, J. M. D. 2015, MNRAS, 454, 1658
Kruijssen, J. M. D. 2019, MNRAS, 486, L20
Kruijssen, J. M. D. & Lamers, H. J. G. L. M. 2008, A&A, 490, 151
Kruijssen, J. M. D., Maschberger, T., Moeckel, N., et al. 2012, MNRAS, 419, 841
Kruijssen, J. M. D., Pelupessy, F. I., Lamers, H. J. G. L. M., Portegies Zwart, S. F., & Icke, V. 2011, MNRAS, 414, 1339
Kruijssen, J. M. D., Pfeffer, J. L., Crain, R. A., & Bastian, N. 2019a, MNRAS, 486, 3134
Kruijssen, J. M. D., Pfeffer, J. L., Reina-Campos, M., Crain, R. A., & Bastian, N. 2019b, MNRAS, 486, 3180
Kruijssen, J. M. D., Schruba, A., Chevance, M., et al. 2019c, Nature, 569, 519
Krumholz, M. R. & McKee, C. F. 2005, ApJ, 630, 250
Kundic, T. & Ostriker, J. P. 1995, ApJ, 438, 702
Lacey, C. & Cole, S. 1993, MNRAS, 262, 627
Lahén, N., Naab, T., Johansson, P. H., et al. 2020, ApJ, 891, 2
Li, H. & Gnedin, O. Y. 2019, MNRAS, 486, 4030
Li, H., Gnedin, O. Y., & Gnedin, N. Y. 2018, ApJ, 861, 107
Li, H., Gnedin, O. Y., Gnedin, N. Y., et al. 2017, ApJ, 834, 69
Li, H., Vogelsberger, M., Bryan, G. L., et al. 2022, MNRAS, 514, 265
Lian, J., Wang, T., Feng, Q., Huang, Y., & Guo, H. 2025, ApJ, 990, L37
Licquia, T. C. & Newman, J. A. 2015, ApJ, 806, 96
Ma, X., Grudić, M. Y., Quataert, E., et al. 2020, MNRAS, 493, 4315
Maccarone, T. J., Kundu, A., Zepf, S. E., & Rhode, K. L. 2007, Nature, 445, 183
Maccarone, T. J., Kundu, A., Zepf, S. E., & Rhode, K. L. 2011, MNRAS, 410, 1655
Mandelker, N., Dekel, A., Ceverino, D., et al. 2014, MNRAS, 443, 3675
Marinacci, F., Pakmor, R., & Springel, V. 2014, MNRAS, 437, 1750
Marinacci, F., Sales, L. V., Vogelsberger, M., Torrey, P., & Springel, V. 2019, MNRAS, 489, 4233
Massari, D., Koppelman, H. H., & Helmi, A. 2019, A&A, 630, L4
Mowla, L., Iyer, K., Asada, Y., et al. 2024, Nature, 636, 332
Murali, C. & Weinberg, M. D. 1997a, MNRAS, 291, 717
Murali, C. & Weinberg, M. D. 1997b, MNRAS, 288, 767
Murali, C. & Weinberg, M. D. 1997c, MNRAS, 288, 749
Murray, N. 2011, ApJ, 729, 133
Newton, O., Davies, J. J., Pfeffer, J., et al. 2025, MNRAS, 542, 591
Ostriker, J. P., Spitzer, Jr., L., & Chevalier, R. A. 1972, ApJ, 176, L51
Pakmor, R., Bieri, R., Fragkoudi, F., et al. 2025a, arXiv e-prints, arXiv:2507.13440
Pakmor, R., Fragkoudi, F., Grand, R. J. J., et al. 2025b, MNRAS, 543, 4355
Pakmor, R., Gómez, F. A., Grand, R. J. J., et al. 2017, MNRAS, 469, 3185
Pascale, R., Calura, F., Vesperini, E., et al. 2025, A&A, 699, A31
Pfeffer, J., Kruijssen, J. M. D., Crain, R. A., & Bastian, N. 2018, MNRAS, 475, 4309
Pfeffer, J. L., Trujillo-Gomez, S., Kruijssen, J. M. D., et al. 2020, MNRAS, 499, 4863
Phipps, F., Khochfar, S., Varri, A. L., & Dalla Vecchia, C. 2020, A&A, 641, A132
Planck Collaboration, Ade, P. A. R., Aghanim, N., et al. 2014, A&A, 571, A16
Plummer, H. C. 1911, MNRAS, 71, 460
Portegies Zwart, S. F., McMillan, S. L. W., & Gieles, M. 2010, ARA&A, 48, 431
Prieto, J. L. & Gnedin, O. Y. 2008, ApJ, 689, 919
Reina-Campos, M., Keller, B. W., Kruijssen, J. M. D., et al. 2022a, MNRAS, 517, 3144
Reina-Campos, M. & Kruijssen, J. M. D. 2017, MNRAS, 469, 1282
Reina-Campos, M., Sills, A., & Bichon, G. 2023, MNRAS, 524, 968
Reina-Campos, M., Trujillo-Gomez, S., Deason, A. J., et al. 2022b, MNRAS, 513, 3925
Renaud, F., Agertz, O., & Gieles, M. 2017, MNRAS, 465, 3622
Renaud, F., Boily, C. M., Naab, T., & Theis, C. 2009, ApJ, 706, 67
Renaud, F., Bournaud, F., & Duc, P.-A. 2015, MNRAS, 446, 2038
Renaud, F., Bournaud, F., Kraljic, K., & Duc, P. A. 2014, MNRAS, 442, L33
Rodriguez, C. L., Hafen, Z., Grudić, M. Y., et al. 2023, MNRAS, 521, 124
Saracino, S., Kamann, S., Guarcello, M. G., et al. 2022, MNRAS, 511, 2914
Schaal, K. & Springel, V. 2015, MNRAS, 446, 3992
Schaal, K., Springel, V., Pakmor, R., et al. 2016, MNRAS, 461, 4441
Schaye, J. 2004, ApJ, 609, 667
Schaye, J., Crain, R. A., Bower, R. G., et al. 2015, MNRAS, 446, 521
Schaye, J. & Dalla Vecchia, C. 2008, MNRAS, 383, 1210
Schechter, P. 1976, ApJ, 203, 297
Searle, L. & Zinn, R. 1978, ApJ, 225, 357
Sick, J., Courteau, S., Cuillandre, J.-C., et al. 2015, in IAU Symposium, Vol. 311, Galaxy Masses as Constraints of Formation Models, ed. M. Cappellari & S. Courteau, 82–85
Snaith, O., Haywood, M., Di Matteo, P., et al. 2015, A&A, 578, A87
Spitler, L. R. & Forbes, D. A. 2009, MNRAS, 392, L1
Spitzer, L. 1987, Dynamical evolution of globular clusters
Springel, V. 2005, MNRAS, 364, 1105
Springel, V. 2010, MNRAS, 401, 791
Springel, V. & Hernquist, L. 2003, MNRAS, 339, 289
Strader, J., Brodie, J. P., Cenarro, A. J., Beasley, M. A., & Forbes, D. A. 2005, AJ, 130, 1315
Sun, J., Leroy, A. K., Ostriker, E. C., et al. 2023, ApJ, 945, L19
Taylor, E. D., Read, J. I., Orkney, M. D. A., et al. 2025, Nature, 645, 327
Toomre, A. 1964, ApJ, 139, 1217
Usher, C., Caldwell, N., & Cabrera-Ziri, I. 2024, MNRAS, 528, 6010
Utomo, D., Sun, J., Leroy, A. K., et al. 2018, ApJ, 861, L18
Valenzuela, L. M., Forbes, D. A., & Remus, R.-S. 2025, MNRAS, 537, 306
Valenzuela, L. M., Moster, B. P., Remus, R.-S., O'Leary, J. A., & Burkert, A. 2021, MNRAS, 505, 5815
VandenBerg, D. A., Brogaard, K., Leaman, R., & Casagrande, L. 2013, ApJ, 775, 134
Vesperini, E. 2001, MNRAS, 322, 247
Villanueva-Domingo, P., Villaescusa-Navarro, F., Genel, S., et al. 2023, Phys. Rev. D, 107, 103003
Vogelsberger, M., Genel, S., Sijacki, D., et al. 2013, MNRAS, 436, 3031
Wadsley, J. W., Veeravalli, G., & Couchman, H. M. P. 2008, MNRAS, 387, 427
Wainer, T. M., Johnson, L. C., Seth, A. C., et al. 2022, ApJ, 928, 15
Weatherford, N. C., Chatterjee, S., Kremer, K., & Rasio, F. A. 2020, ApJ, 898, 162
Weinberg, M. D. 1994a, AJ, 108, 1414
Weinberg, M. D. 1994b, AJ, 108, 1403
Weinberg, M. D. 1994c, AJ, 108, 1398
Whitmore, B. C., Chandar, R., Schweizer, F., et al. 2010, AJ, 140, 75
Whitmore, B. C. & Schweizer, F. 1995, AJ, 109, 960
Williams, B. F., Dolphin, A. E., Dalcanton, J. J., et al. 2017, ApJ, 846, 145
Williams, C. E., Naoz, S., Lake, W., et al. 2025, ApJ, 990, 135
Zepf, S. E., Ashman, K. M., English, J., Freeman, K. C., & Sharples, R. M. 1999, AJ, 118, 752
Zhang, Q. & Fall, S. M. 1999, ApJ, 527, L81

Table A.1: Additional variations for halo 6.

Model	Variation	Variation remarks
Resolution level 4 ($M_{\rm bary} \sim 5\times10^4 M_\odot$, $\epsilon_{\rm phys} \sim 375$ pc)		
x50in100myr	Enhanced shocks	x50 during 100 Myr
x50in200myr	Enhanced shocks	x50 during 200 Myr
x50fullevo	Enhanced shocks	x50 full evolution
Resolution level 5 ($M_{\rm bary} \sim 4\times10^5 M_\odot$, $\epsilon_{\rm phys} \sim 750$ pc)		
Full tensor	With long range forces	$T_{ij} = T_{ij,\rm Tree} + T_{ij,\rm PM}$
rhevo_f1/2	$f = 1/2$ in eq. 22	$(dr_{\rm h})_{\rm sh} = 0$; $(d\rho_{\rm h})_{\rm sh} < 0$
rhevo_f1	$f = 1$ in eq. 22	$(dr_{\rm h})_{\rm sh} < 0$; $(d\rho_{\rm h})_{\rm sh} > 0$

Notes. The columns are (i) the model variation identifier, and (ii) and (iii) the model variation description.

Appendix A: Additional variation model runs

For the appendix, some other model variations have been run at the same or lower resolution for the halo 6. These are summarized on the table A.1.

Appendix B: Tidal Tensor

B.1. Tidal Tensor Calculus

As the formation and evolution of the SCs in this model is heavily reliant on the tidal tensor, ensuring that its calculus is correct becomes fundamental. We reproduce the test included in both Pfeffer et al. (2018) and Reina-Campos et al. (2022a) for obtaining the tidal tensor on a Plummer (1911) sphere in fig. B.1. The same sphere of total mass $M = 10^{11}\mathrm{M}_\odot$ and $N = 10^6$ particles used by Reina-Campos et al. (2022a) was run. Their initial distribution is described by the Plummer potential,

$$\Phi_{\rm PL}(r) = -\frac{GM}{\sqrt{r^2 - r_c^2}}. \tag{B.1}$$

The ensemble of particles is run for $\sim$ 1 Gyr and, after relaxation, evolves to a characteristic radius of $r_c \simeq 1.82$ kpc. In fig. B.1, the distribution of the numerical first eigenvalue, as obtained from the particles distribution, is compared to the analytical, expected, eigenvalue which is

$$T_{\rm rr} = -\frac{\partial^2 \Phi_{\rm PL}}{\partial r^2} = -GM\frac{r_c^2 - 2r^2}{(r^2 + r_c^2)^{5/2}}. \tag{B.2}$$

It is evident that the median eigenvalue follows the expected analytical solution within the standard deviation of the particles.

B.2. Long range contributions

Additionally, in section 2 was mentioned that the long range force contributions to the tidal tensor are not taken into account as they are minimal and should not influence whether the medium is compressive or not. Furthermore, the tidal shocks mass loss evolution should not be sensitive to these contributions. Here we put this to test by running two simulations of the fiducial model of AuriGLOBES at resolution "level 5" for the halo 6. The first run without including the long-range force contributions to the tidal tensor (`Fiducial` model), and the second one (`Full tensor`) including them by means of differentiating the Poisson equation in Fourier space (by "pulling down" $k's$), i.e.

$$\Phi(\mathbf{k}) \propto \frac{\delta(\mathbf{k})}{k^2} \Longrightarrow \widetilde{T}_{ij}(\mathbf{k}) \propto \frac{k_i k_j}{k^2}\delta(\mathbf{k}),$$

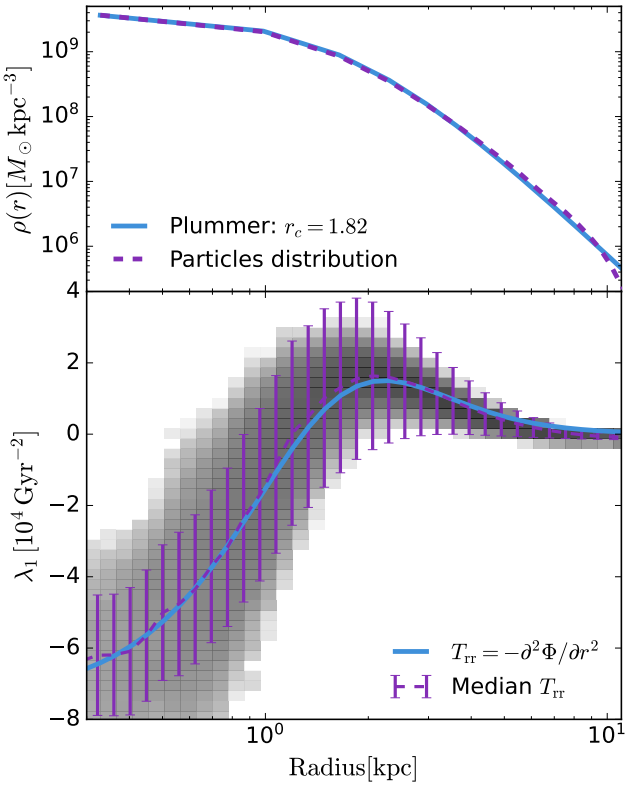


Fig. B.1: Tidal tensor from a simulated Plummer sphere. *Top*: Profile fit of the simulated sphere. *Bottom*: Distribution of the highest tidal tensor eigenvalue, as calculated in the simulation compared to the analytical eigenvalue.

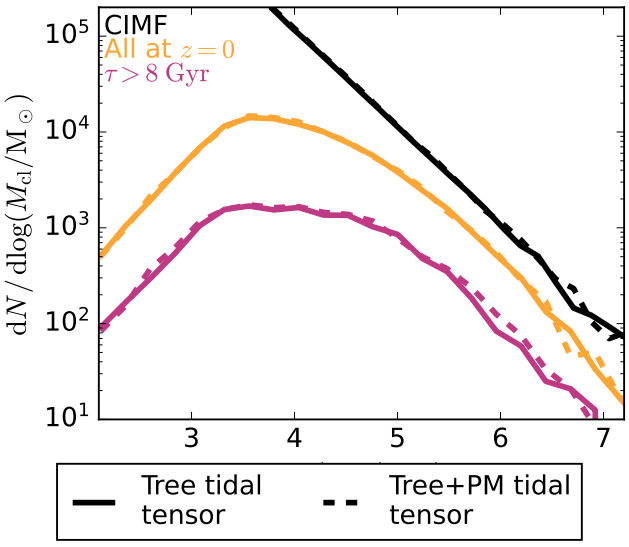


Fig. B.2: Mass functions for the simulated SC populations when including long range contributions in the calculus of the tidal tensor.

where $\delta(\mathbf{k})$ is the density contrast field.

The simulated GCMFs for both simulations are shown in fig. B.2. It can be seen that, down to the $\tau > 8$ Gyr age cut, they are nearly identical with their differences relying on the differences of the CIMF. This mainly shows that the effect on the mass loss evolution is in fact minimal. At formation, however, there is a

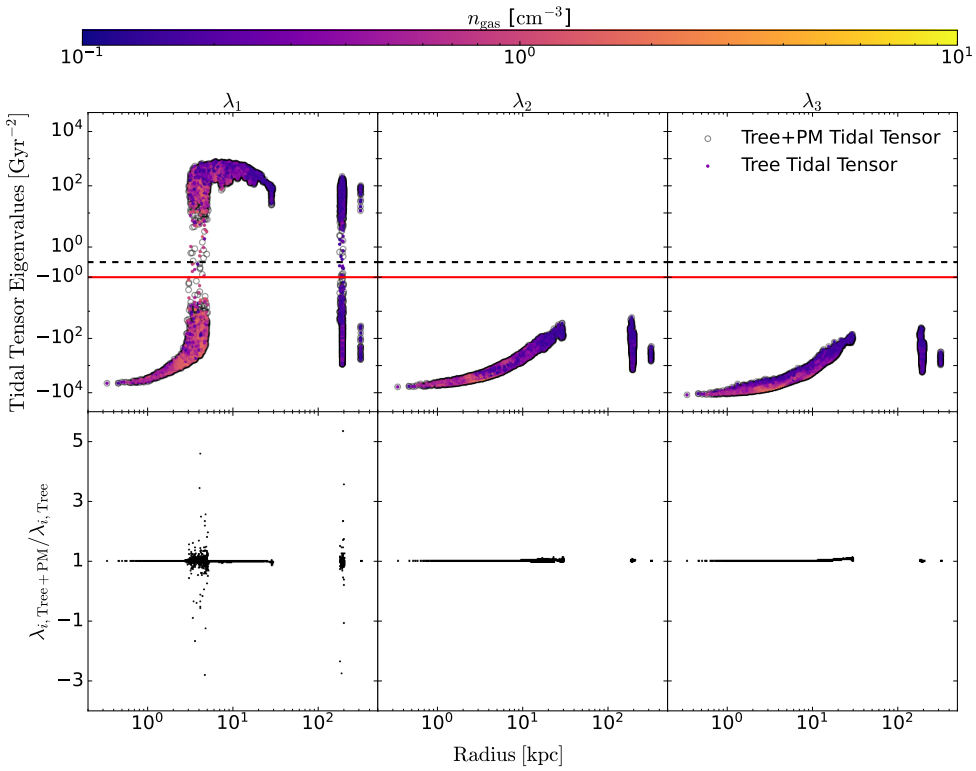


Fig. B.3: Star forming gas tidal tensor eigenvalues distribution at $z = 0$, for the halo 6. *Top*: Distribution for the `Fiducial` variation at lower resolution with/without including the tidal tensor from long-range gravity contributions. *Bottom*: Ratio of the eigenvalues for the two different calculations of the tidal tensor.

minimal effect on the amount of clusters being formed. This can be verified on fig. B.3, by comparing the tidal tensor eigenvalues of star forming gas at redshift $z = 0$ for both simulations. Although the distribution is nearly identical, close to the zero crossing, and to our numerical threshold to define a tidally compressive region, there are differences on some cells lying above or below this line. Therefore, SCs that were formed in some environments at one variation, may not be formed in the other. Nevertheless, this test shows that neglecting the long-range force contributions to the tidal tensor is justified given that including it increases the computational time by ~ 70 % and the effect in the simulated populations is minimal.

B.3. Estimating Ω and κ

The circular frequency, Ω, and the epicyclic frequency, κ, are quantities estimated locally in order to calculate properties both at the formation (equations 7 and 5), and evolution (equation 16), of the SCs. Here we demonstrate that the estimate of these quantities from the tidal tensor agrees well with the values calculated at post-processing. The circular and epicyclic frequencies can be derived from the tidal tensor eigenvalues via

$$\Omega^2 = \frac{1}{3}\left|\sum_i \lambda_i\right|, \tag{B.3}$$

and

$$\kappa^2 = \left|3\Omega^2 - \lambda_1\right|. \tag{B.4}$$

With λ_1 being the first (maximal) eigenvalue of the tidal tensor. These relations are derived from equating the circular frequency in terms of the mean density enclosed within the radius r, i.e. $\Omega^2 = v_c^2/r^2 = GM(r)/r^3 = 4/3\pi G\bar{\rho}(r)$, to the Poisson's equation and its relation with the tidal tensor eigenvalues, $\nabla^2\Phi = 4\pi G\rho = -\sum_i \lambda_i$. For the full derivation, we refer the interested reader to the appendix A of Pfeffer et al. (2018) or to the appendix C in Reina-Campos et al. (2022a).

We compare in fig. B.4 the distribution of the enclosed mean density, $\bar{\rho}$, the circular frequency, Ω, and epicylic frequency, κ, as estimated from the tidal tensor eigenvalues to the quantities calculated at post processing from the simulated halo 6 at $z = 0$. The plotted distribution of the estimated values corresponds to stars formed in the last 50 Myr of the galaxy evolution. It is evident from the figure that the estimate is in an overall agreement with the profile of the simulated galaxy. The bigger differences are in the central ~ 500 pc of the galaxy, comparable to the softening length of the simulation, and at larger radii > 10 kpc where the scatter becomes important. Nevertheless, the estimates are reasonable for the purposes of the model.

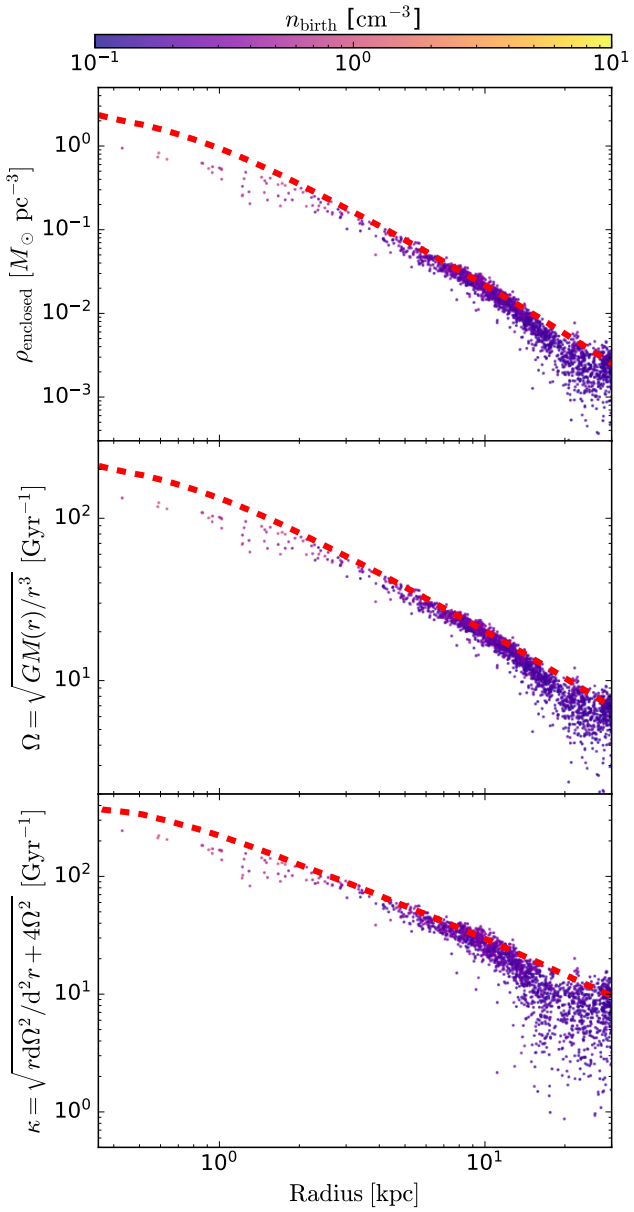


Fig. B.4: Enclosed mean density (*top*), circular frequency (*middle*), and epicyclic frequency (*bottom*) distributions, as estimated from the tidal tensor eigenvalues. The distribution corresponds to stars born during the last 50 Myr of galaxy evolution for the halo 6. The profile, as calculated at post-processing, of these quantities is included in red dashed line in each panel for comparison.

Appendix C: On the r_h evolution model

The fiducial model allows the half-mass radius to change in correspondence to the mass loss that the SCs experience following equation 22. As mentioned in section 2.2, f describes the increase of energy of the remaining bound stars after a tidal shock mass loss event, and how it is related to the density at the half-mass radius, $\rho_{\rm h}$. The particular $f = 3/5$ choice describes the change of $r_{\rm h}$ after tidal shocks mass loss such that $\rho_{\rm h}$ remains constant. Here we test the sensibility of the model to this particular choice by running two variations of the model with choices of $f = 1$, and $f = 1/2$. These choices correspond to $\rho_{\rm h}$ increasing after shock events, potentially shielding SCs from subsequent mass loss, and to no $r_{\rm h}$ change from shock events, experiencing only the overall expansion from stellar evolution and two-body relaxation, respectively. The MFs obtained from these variations, and how they compare to the fiducial choice, are shown in fig. C.1. The MFs are remarkably similar with very small differences with respect to the fiducial $f = 3/5$ choice. The reason behind this behavior could be two-fold:

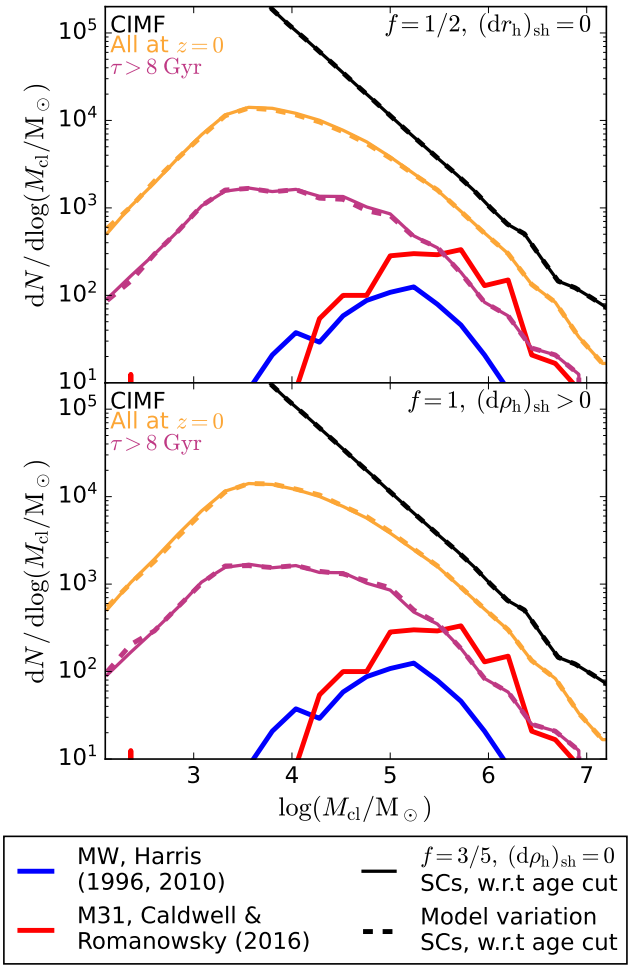


Fig. C.1: Mass functions for the simulated SC populations for different choices of f in the dynamical half-mass radius evolution.

- The strength of the tidal shocks is not sufficiently high to be able to distinguishing among these parameters.
- The change in the half-mass radius due to tidal shocks is subdominant with respect to the change from the enhanced two-body relaxation.

Nevertheless, we keep the $f = 3/5$ choice as a safe spot on trying to keep most physics as can be possible with this model.

Appendix D: Shocks enhancement variations

We further explore the tidal shocks disruption in our model by performing additional variations enhancing the shock-driven mass loss with a higher factor of 50 over different time periods. The MFs produced in this variations are presented in fig. D.1. The top and central panels explore the effect of this enhancement only during the first stages of the SCs evolution, with the aim to

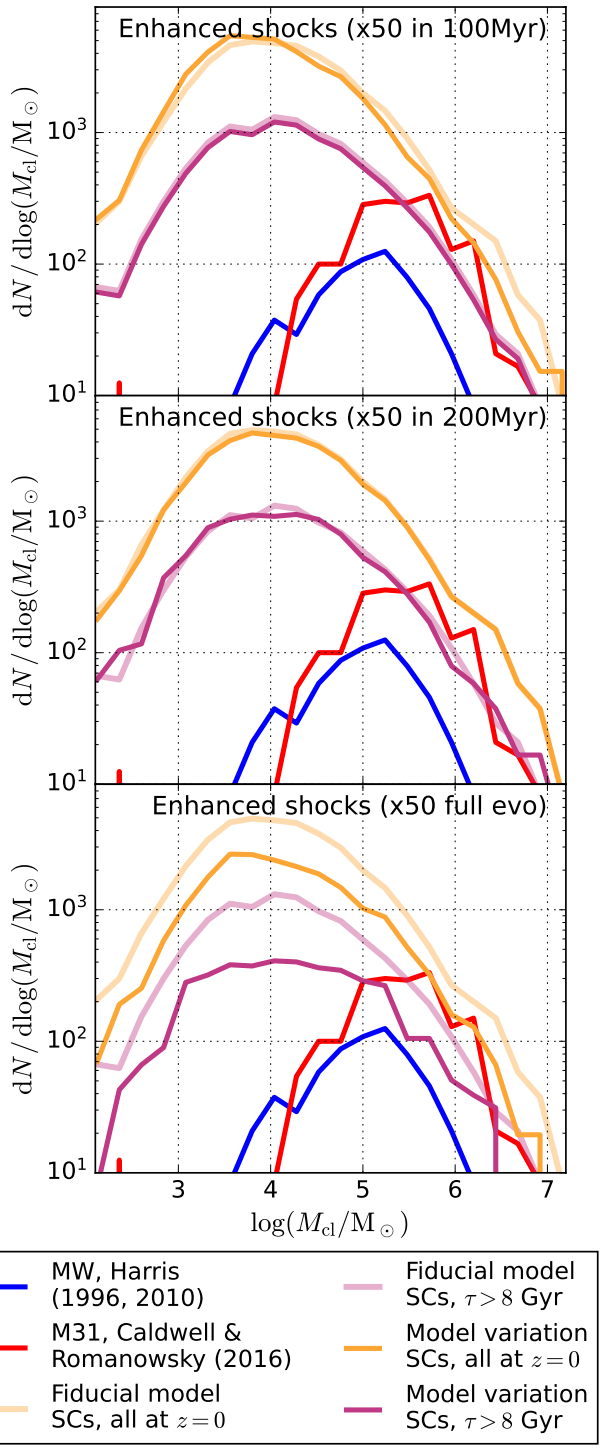


Fig. D.1: Mass functions for the simulated SC populations for the additional shocks enhancement variations.

test how the model is capturing the early disruption from the natal environment (Kruijssen et al. 2012). The duration of the enhancement is based on the typical timescale of this rapid disruption phase quoted in Kruijssen (2015) and De Lucia et al. (2024), i.e. $t_{cce} = 175$ Myr. The effect of this enhancement during these short periods is negligible. This suggests that the SCs that are disrupted in short timescales, i.e. $\tau < 1$ Gyr, in the `Fiducial` model just accelerate their disruption while the effect on the rest of the SCs is minimal given that their lifetime is likely large, i.e. $\tau > 1$ Gyr.

Moving now to keeping this enhancement over a larger period, the MFs in the bottom panel reproduce the same behavior discussed in section 4.1. The normalization is lowered but the peak of the MFs is mostly unchanged with an important population present at the low mass tail of the old ($\tau > 8$ Gyr) population. We interpret here that the size evolution of the SCs acts as an agent suppressing the disruption. In particular, this stronger disruption, expected from e.g. the inclusion of cold phase of the ISM, shields the SCs through their change of half-mass radius.

Appendix E: Individual halo SFR, CFR and age distributions

Finally, we present here a detailed comparison of the different SC age distributions of the simulated halos (bottom panel fig. 9) and their relation with their SFHs. We show in fig. E.1 the individual halo SFH, and SC and GC age distributions in comparison to the SFH of the MW from Snaith et al. (2015), and its GC age distribution as compiled by Kruijssen et al. (2019b). We also include the age distribution of the simulated GCs applying the same metallicity cut as in fig. 10 to target the old populations of each halo. The infall times of the main merger events for the halo are included as vertical dotted lines in each panel. These are identified as having a baryon mass ratio of at least 1:12 at the time of infall, i.e. when the merging system crosses R_{200}. Looking at all the individual SFRs, no simulation has the high early SFR like the MW, i.e. $\sim$ 10–20 $M_\odot\,yr^{-1}$ during the first $\sim$ 4 Gyr of evolution and forming half of its stellar mass (Snaith et al. 2015). Only after the first $\sim$ 2–4 Gyr the simulated SFRs reach values comparable to the estimated SFR of the MW. Furthermore, past this time between $z \simeq$ 1–2, the SFRs of the simulated halos are around an order of magnitude higher than that of the MW. For example, the halos with the oldest peaks in the GC age distribution, and closer to that of the MW, are halo 23 and 24. For these halos, the SFR quickly grows to match the MW SFR at $\approx$ 13 Gyr lookback time and maintains this high SFR until peaking at $z \simeq 2$. The GC age distribution of halo 23 reflects this behavior and peaks at the same $z \simeq 2$ redshift, which is $\approx$ 2 Gyr later than the peak of the Galactic GCs age distribution. Halo 24, similarly shows this peak as well as another at $z \simeq 1$ that correlates with its SFR. This behavior heavily impacts any attempt to reproduce the observed GC age distribution when any of the halos is able to reproduce the MW SFH. In particular, this does not constitute a limitation of the formation prescription, but simply follows from the parent simulation/galaxy formation model.

When looking at GC formation at high redshift, there is a general correlation with merger induced starbursts. This is evident from the GC age distributions with the [Fe/H] < -0.5 metallicity cut. Here, the distributions are consistent with older populations whose peaks follow early accretion events, and are generally closer to the observational one for the MW. In particular, most of the distributions after applying the metallicity cut are correlated with early mergers. This is evidenced with the age distributions peaks coinciding with the infall times of the mergers. We bring the attention to halo 22 here, as the halo that, after the metallicity cut, gives the closest age distribution with respect to the MW. We defer a dedicated analysis of this correlation with the accretion history to future work.

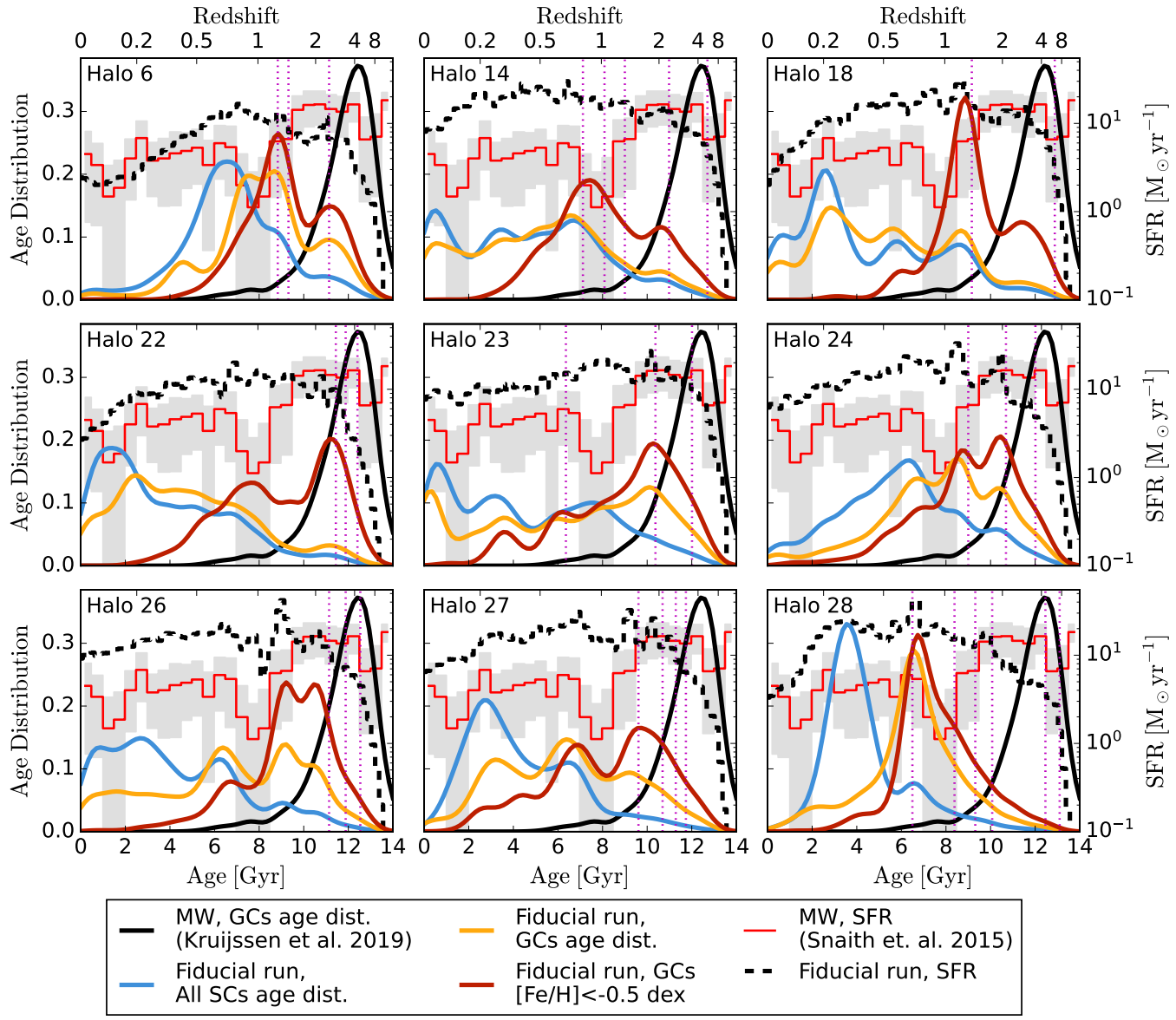


Fig. E.1: Age distribution of the simulated cluster populations for the individual halos. Different age distributions are shown for all SCs, GC selection, and GC selection with a metallicity cut. For comparison, the MW GC age distribution is included. The individual halo SFR is shown and compared to that of the MW from Snaith et al. (2015). The vertical dashed lines denote mergers with a baryon mass ratio of at least 1:12 at infall time.